EARTH SCIENCE & RESOURCE ENGINEERING
www.csiro.au

Improved discretisation and dynamic modelling of CO_2 solubility during injection and subsequent convective dispersion

Christopher P. Green and Jonathan Ennis-King
Report Number EP142875
June 10, 2014

ANLEC project 7-1011-0190

CSIRO Earth Science & Resource Engineering
71 Normanby Road, Clayton VIC, 3168, Australia
Private Bag 10, Clayton South VIC, 3169, Australia
Telephone: +61 3 9545 2777
Fax: +61 3 9545 8380

Copyright and disclaimer

© 2014 CSIRO To the extent permitted by law, all rights are reserved and no part of this publication covered by copyright may be reproduced or copied in any form or by any means except with the written permission of CSIRO.

Important disclaimer

CSIRO advises that the information contained in this publication comprises general statements based on scientific research. The reader is advised and needs to be aware that such information may be incomplete or unable to be used in any specific situation. No reliance or actions must therefore be made on that information without seeking prior expert professional, scientific and technical advice. To the extent permitted by law, CSIRO (including its employees and consultants) excludes all liability to any person for any consequences, including but not limited to all losses, damages, costs, expenses and any other compensation, arising directly or indirectly from using this publication (in part or in whole) and any information or material contained in it.

Acknowledgement

The authors wish to acknowledge financial assistance provided through Australian National Low Emissions Coal Research and Development (ANLEC R&D). ANLEC R&D is supported by Australian Coal Association Low Emissions Technology Limited and the Australian Government through the Clean Energy Initiative.

Contents

1 Executive summary . . . 1

2 Introduction . . . 2

3 Short-term dissolution: the injection period . . . 5

4 Convective mixing in homogeneous media . . . 9

4.1 Governing equations . . . 9

4.2 Isotropic media . . . 10

4.3 Anisotropic media . . . 13

5 Convective mixing in heterogeneous media . . . 15

5.1 Numerical results . . . 16

6 Geochemistry . . . 23

6.1 Background . . . 23

6.2 Technical challenges of flux simulation with geochemistry . . . 24

6.2.1 Grid refinement . . . 25

6.2.2 Conclusions on technical challenges . . . 27

6.3 Geochemical model for Precipice Sandstone . . . 28

6.4 Coupling convection and geochemistry in Precipice Sandstone . . . 28

6.5 Conclusions for geochemistry . . . 29

7 Sub-grid scale model of convective mixing . . . 31

7.1 Theory . . . 32

7.2 Numerical results . . . 34

8 Conclusions . . . 42

1 Executive summary

Numerical simulations are an essential tool for assessing the long-term storage of CO_2 in saline aquifers, such as the proposed pilot project at the Wandoan site in Queensland's Surat Basin. However, the robustness of the numerical predictions is dependent on accurately capturing the essential physical processes involved. One of the most significant results obtained through numerical simulations is the partitioning of CO_2 into immobile phases, particularly the amount immobilised at residual saturation and the amount that has dissolved into the resident formation water. The quantity and time scale for CO_2 immobilised in this manner is critical for understanding the security of the geological storage, as it reduces the possibility of leakage into shallower formations.

It is well known that the necessary use of large grid blocks in numerical simulations of field-size projects introduces errors in the predictions of the amount of dissolved CO_2. In the injection stage of a storage project, grid blocks that are too large will result in an overestimate of the amount of CO_2 dissolved in the formation brine. Recent work has considered this problem and provided simple solutions to correct this error based on a geometric scaling argument (Green and Ennis-King, 2012).

During the later stage of a storage project, where density-driven convective mixing can significantly enhance the amount of CO_2 that is dissolved, the use of large grid blocks can lead to numerical predictions that significantly underestimate the amount of dissolved CO_2. This is primarily due to disparate length scales between the coarse grid blocks often necessary in a field-scale simulation, and the convective mixing process which can take place on a scale that can be several orders of magnitude smaller than the size of such coarse grid blocks. The fine-scale convective mixing process has been the subject of a large body of scientific literature in recent years. Unfortunately, methods are lacking to include this effect in field-scale simulations, such as those that will be required for storage in the Precipice Sandstone in the Surat (e.g. the Wandoan site).

This study addresses some of the shortcomings in the scientific literature regarding the effect of coarse grids on the convective mixing process. An important estimate of the long-term stable mass flux during steady convective mixing is extended to the case of an anisotropic homogeneous reservoir, which is shown to provide an adequate representation of a heterogenous model using flow barriers to introduce vertical heterogeneity.

The effects of the spatial grid on the contribution to the convective mixing process due to geochemical reactions in the reservoir are also considered. In the two cases studied, one based on the Frio formation and the other on the Precipice Sandstone, the inclusion of geochemistry increased the dissolution flux by a factor of 3 when ionic concentrations were coupled to fluid density. A means of upscaling these effects was suggested through changes to the fluid density term.

Finally, a scheme for correcting the observed error in the convection-enhanced dissolution based on grid-corrected fluid or reservoir properties is proposed. Numerical results demonstrate how this correction can be applied in practice to significantly reduce the error in the numerical predictions of the amount of CO_2 that is immobilised due to dissolution.

Current field-scale simulation models underestimate the rate of CO_2 dissolution in saline formations, due to grid coarseness and the omission of geochemical effects. For storage in the Precipice Sandstone, this leads to overestimate of the risk of leakage. The results obtained in this project can be implemented in commercial simulation software to improve the modelling of the short-term and long-term behaviour of injected carbon dioxide. Better models (with upscaling of the effects of convection and geochemistry) will reduce the project risk by improving estimates of CO_2 dissolution and long-term storage security.

2 Introduction

Geological storage of carbon dioxide is one of the possible strategies currently being explored as a means to reduce anthropomorphic emission of greenhouse gases. It is the subject of extensive scientific research worldwide, with a corresponding large body of published literature.

One of the most likely storage options is sequestration in deep saline aquifers (van der Meer, 1992; Bachu et al., 1994), where CO_2 is injected into the resident formation brine. Storage security can be achieved through several mechanisms. The most commonly considered storage mechanism is structural trapping, where an impermeable caprock forms a structural closure that prevents buoyant migration of injected CO_2 beyond the caprock.

In the case where CO_2 is injected into a saline aquifer with a bounding cap rock, buoyancy drives vertical migration of the mobile CO_2 (CO_2 in the supercritical gas phase), which then spreads beneath the cap rock to form a thin, laterally extensive plume of gas phase CO_2, see Figure 2.1. In time, the gaseous CO_2 begins to dissolve into the local formation water, leading to a small increase in density of the saturated brine at the top of the aquifer. Diffusion of the dissolved CO_2 allows further dissolution, a process that leads to a gravitational instability whereby a denser fluid lies atop a less dense one. This process is known as convection, where motion is induced as vertical acceleration overcomes diffusion. Weir et al. (1996) first observed the formation of a convection cell during numerical simulations of CO_2 storage in a deep saline aquifer.

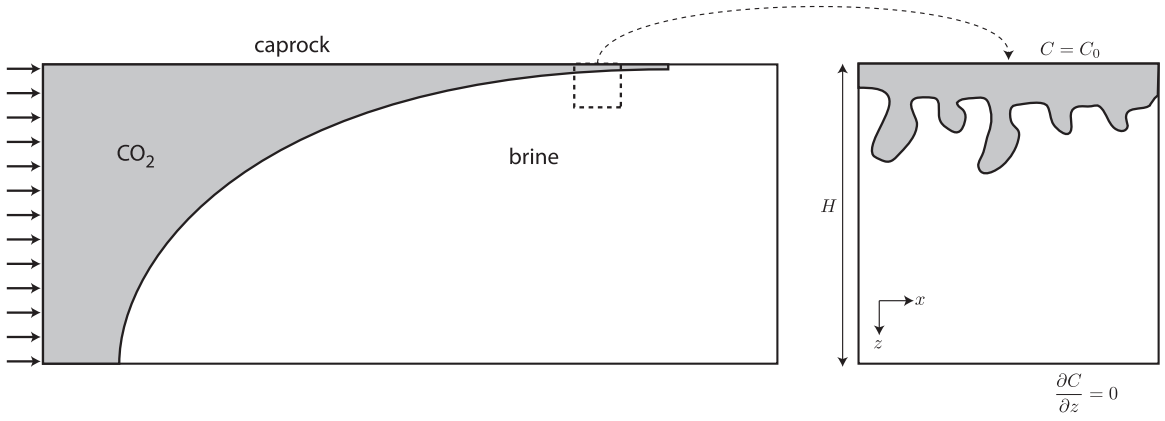

Figure 2.1: Schematic of the CO_2 injection in a horizontal reservoir bounded by an impermeable caprock. The shaded region represents CO_2 in the mobile (supercritical) gas phase, which migrates upwards and spreads beneath the caprock. The close up view of the dashed box shows the commonly used model for studies of the convective mixing process.

Shortly after Weir et al. (1996), Lindeberg and Wessel-Berg (1997) explicitly considered both temperature and density-driven convection of a plume of CO_2 lying atop brine. Using a simplified approach based on well-known methods for analysing temperature-driven convection in porous media, they presented a basic stability criteria for the onset of convection. Lindeberg and Wessel-Berg (1997) noted that convection could drive the dissolution rate faster than diffusion alone, making it an important mechanism for the safe storage of CO_2 in geological formations.

Fine-scale numerical studies by Lindeberg and Bergmo (2003), Ennis-King and Paterson (2003), and Ennis-King and Paterson (2005) verified the presence of convection, with the now-familiar fingers of CO_2 saturated brine sinking deep into the unsaturated brine modelled in detail numerically, and observed experimentally. These studies demonstrated that the rate of dissolution of gaseous CO_2 into the formation brine accelerates sharply at the onset of convective mixing, suggesting that convective

mixing has an important role in the safe long-term storage of CO_2 in saline aquifers.

An example of the onset of convection and the subsequent formation of downwelling fingers of dissolved CO_2 obtained from high resolution numerical simulations is presented in Figure 2.2. Initially, mass transfer from the saturated region into the underlying unsaturated reservoir is due to diffusion only, see Figure 2.2(a). After a finite incubation time, the gravity instability due to the density difference results in the formation of the characteristic convective fingers, see Figure 2.2(b). As time increases, the fingers grow and merge in a complex fashion, forming fewer but larger fingers, see Figure 2.2(c). This process continues as the fingers continue to grow, accelerating the dissolution of CO_2 at the top of the reservoir and transporting it deep into the reservoir, see Figure 2.2(d).

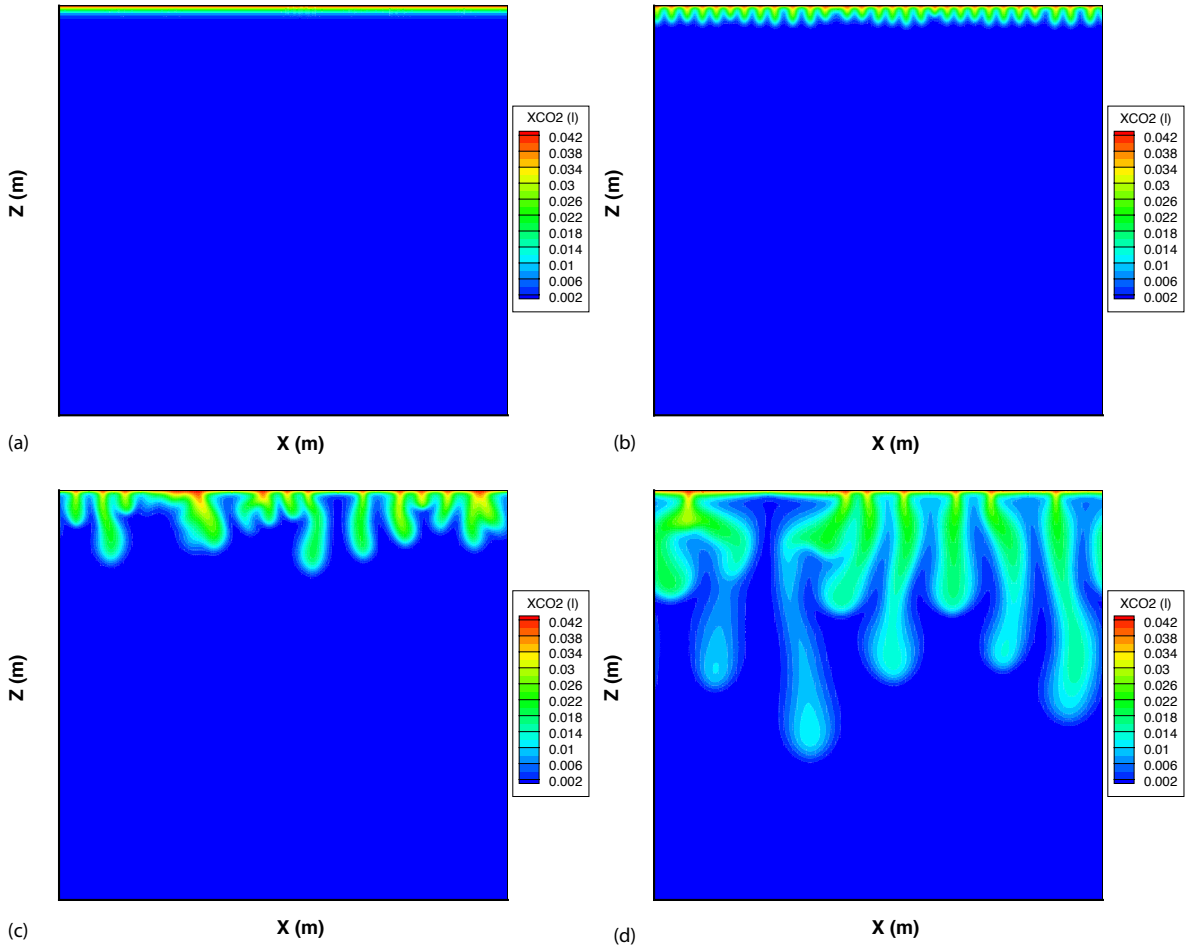

Figure 2.2: Dissolved CO_2 mass fraction during the convective mixing process. Time increases from (a) to (d). (a) Initial mass transfer is by diffusion only; (b) Gravity instability results in fingers; (c) Fingers grow and merge; (d) Large fingers transport CO_2 deep into the reservoir.

One aspect of geological storage of CO_2 that is commonly calculated by numerical simulations is the dissolution of CO_2 into the formation brine, which has an important role in trapping large quantities of injected CO_2. The amount of dissolution in a saline aquifer, however, has been observed to be strongly affected by the resolution of the spatial grid (Ennis-King et al. (2003); Ennis-King and Paterson (2002)). This effect has been observed for both short-term (up to tens of years) and longer-term results (up to thousands of years).

For short-term results, the amount of dissolved CO_2 calculated using a coarse computational grid has been shown to overestimate the fine-scale results (Ennis-King et al. (2003); Ennis-King and Paterson

(2002)). As demonstrated by Green and Ennis-King (2012), this error is primarily due to the finite size of the computational grid blocks at the invading saturation front, and is a manifestation of numerical dispersion. Due to the assumption of instantaneous equilibrium between phases in each computational cell, the CO_2 in the gaseous phase at the saturation front has a larger volume of formation brine in which to dissolve for coarsely gridded models than it would have for models using a finer computational mesh. As a result, the amount of CO_2 that can dissolve in the grid blocks at the saturation front is greater for coarse grids than for fine grids. As the size of the grid blocks increases, the proportion of CO_2 dissolved increases correspondingly. This effect is particularly prominent in three-dimensional numerical simulations with coarse grids.

For long-term results, coarse-scale computational grids have been observed to underestimate the amount of dissolved CO_2, in contrast to the short-term results (Ennis-King et al. (2003); Ennis-King and Paterson (2002)). During long-term storage of CO_2 in saline aquifers, it is well known that convective mixing acts to accelerate dissolution of CO_2 (Ennis-King et al. (2005)). This process occurs on a length scale several orders of magnitude smaller than the size of the aquifer, which poses a problem for numerical simulations, where the spatial grid resolution is typically not sufficiently refined to capture this behaviour. This is especially true in three-dimensional simulations, where coarse meshes are often used by necessity. Here, the primary effect of grid coarseness is to inhibit the onset of convection, so that the long-term results will underestimate the dissolution of carbon dioxide Ennis-King et al. (2003); Ennis-King and Paterson (2002). The error in CO_2 dissolution due to the finite-sized grid blocks at the saturation front discussed above for short-term results, which acts to overestimate dissolution, is therefore only a secondary effect in long-term simulations, where the error is dominated by the delayed onset of convective mixing.

It is therefore apparent that methods to improve the numerical predictions of CO_2 dissolution in saline aquifers using finite sized computational grids will be different for short-term results, where the primary source of the error is numerical dispersion at the saturation front, and for long-term results, where the primary source of error is the suppression of density-driven convection.

In this report, we consider the effects of numerical grid on the dissolution of CO_2 into the formation brine of a saline aquifer. To begin, we summarise the recent results of Green and Ennis-King (2012) for correcting the short-term dissolution predictions during the injection period. Following this, we consider the effect of the spatial grid on the long-term numerical predictions of dissolved CO_2, and in particular, the retardation of convective mixing. We extend current theoretical estimates of the long-term average mass flux for isotropic reservoirs to anisotropic reservoirs, and also consider the effect of grid size on mass flux, including the role of geochemistry. Finally, we detail strategies to account for the enhanced dissolution due to subgrid-scale convective mixing in coarse-scale simulation models, and demonstrate how they can be implemented to reduce the error in numerical predictions of CO_2 dissolution.

3 Short-term dissolution: the injection period

The error in the short-term numerical predictions of CO_2 dissolution has previously been considered by Green and Ennis-King (2012), the results of which are briefly summarised here.

To begin, consider the amount of CO_2 dissolved in the brine with a finite number of computational cells, x_c, and compare it to the amount of CO_2 dissolved in the limit of an infinite number of cells, $x_{c,\infty}$. Assuming the solubility of CO_2 does not vary significantly due to changes in salinity or temperature across the plume, solubility can be estimated as $x_{c,\infty}/V_{p,\infty}$ where $V_{p,\infty}$ is the pore volume of the entire plume in the limit of an infinite number of cells (i.e. the sum of grid block volume times porosity over the domain of non-zero CO_2 gas saturation). As numerical dispersion acts to smear the saturation front, the pore volume of the plume calculated using a finite number of grid blocks, V_p, is greater than $V_{p,\infty}$ by an amount well approximated by the pore volume of the grid blocks defining the saturation front, V_f (see Fig. 3.1 for an example for two-dimensional radial flow from a single injection well). It then follows that

$$x_{c,\infty} = x_c \left(1 - \frac{V_f}{V_p}\right). \tag{3.1}$$

For plumes that span a large number of computational grid blocks, $V_f/V_p < 1$, and Eq. (3.1) enables the amount of CO_2 dissolved calculated using finite-sized grid blocks to be corrected. For plumes confined to only a small number of grid blocks however, this correction overestimates the error in x_c. Indeed, in the limit of a plume confined to a single grid block (in which case $V_f = V_p$), Eq. (3.1) predicts that no CO_2 will be dissolved, which is an unrealistic result. As a consequence of this, Eq. (3.1) introduces a dramatic overcorrection for small times.

In order to obtain a robust correction free from this erroneous behaviour, a non-zero value for the amount of dissolved CO_2 as $V_f/V_p \to 1$ must be enforced. In keeping with the concept of the geometrically based scaling discussed so far, it was assumed that $x_{c,\infty} \to x_c/2$ in the limit $V_f \to V_p$, which corresponds to approximating the error in the plume volume by half the total volume of the grid bock on average (i.e. as the actual plume volume will grow from zero initially to the total grid block volume eventually, the error will be half the grid block volume on average). Arguments for other values in this limit can also be made, depending on the level of complexity desired. The choice of $x_{c,\infty} \to x_c/2$ in the limit $V_f \to V_p$ does have the benefit of mathematical convenience, which shall be shown below. Additionally, this limit is of less interest in practice, as large injection rates commonly used rapidly fill a large number of computational grid blocks.

A simple function with the appropriate leading order behaviour in the limits of $V_f \to V_p$ and $V_f \to 0$ can be constructed, and is given by

$$x_{c,\infty} = \frac{x_c}{1 + \dfrac{V_f}{V_p}}. \tag{3.2}$$

It is evident that the choice of $x_{c,\infty} \to x_c/2$ in the limit $V_f \to V_p$ allows for a correction with the simplicity of Eq. (3.1) but with improved behaviour as the number of grid blocks spanned by the plume decreases.

Equation (3.2) is the desired result, providing a simple means for correcting the amount of CO_2 dissolved in the formation water calculated in simulations using finite-sized grid blocks.

In a similar fashion, the CO_2 still in the gaseous phase for finite and infinite numbers of computational

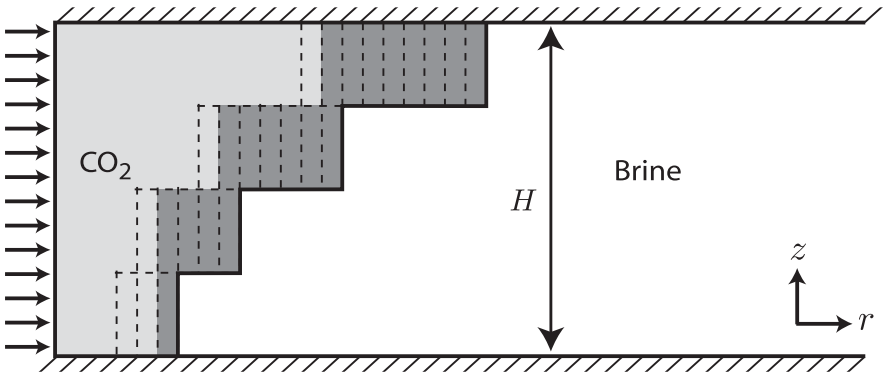

Figure 3.1: Schematic of front volume (dark cells) for radial flow from a single injection well. Part of the two-dimensional radial spatial mesh is also included (dashed lines)

cells, y_c and $y_{c,\infty}$ respectively, are related by

$$y_{c,\infty} = \frac{y_c + \dfrac{V_f}{V_p}(x_c + y_c)}{1 + \dfrac{V_f}{V_p}}. \tag{3.3}$$

If the average porosity is only weakly varying across the plume, then the porosity will cancel between the pore volumes V_p and V_f, so that these equations still holds if grid-block volumes are substituted for pore volumes. In the heterogeneous case where porosity is strongly varying, these volumes should be taken as pore volumes.

Numerical simulation results provide x_c and y_c. Calculation of the ratio of the volume of the saturation front to the total volume containing CO_2 in the gaseous phase, which is straightforward computationally, allows the additional amount of dissolved CO_2 due to finite-scale grid blocks, to be effectively removed through the use of Eqs. (3.2) and (3.3).

The application of the correction provided by Eq. (3.2) can be verified and assessed by comparing numerical results obtained using both coarse and fine-scale grids. Green and Ennis-King (2012). This is illustrated using a simple model of radial flow from a single injection well in a homogeneous and isotropic reservoir, with the effect of gravity included. This was chosen for its simplicity, and for the fact that it allows for simulation using both two-dimensional radial and three-dimensional Cartesian computational grids. Comparison between extremely fine-scale 2D and coarse-scale 3D simulation results is therefore possible in this instance.

For the two-dimensional radial model, the grid was refined until the dissolved mass fraction curve converged to within 1%. In the absence of an analytical solution, this result is used as the 'exact' solution in the subsequent comparisons. This was obtained with a regular radial grid of 40 000 blocks, with lateral spacing of 20 m and vertical resolution of 1 m. In contrast, the three-dimensional Cartesian grid blocks were 320 m in each lateral direction, and 10 m in the vertical direction, with a total of 6250 blocks in one quadrant.

The effect of the spatial grid size on the amount of CO_2 dissolved is clearly demonstrated in Fig. 3.2. The proportion of dissolved CO_2 calculated using the coarse-scale 3D model overestimates the fine-scale 2D results by at least 50% of the 2D result over the entire injection period. Although the absolute error in the two results is only approximately 3% after 30 years of injection, this corresponds to quite a large amount of CO_2 (nearly three million tonnes).

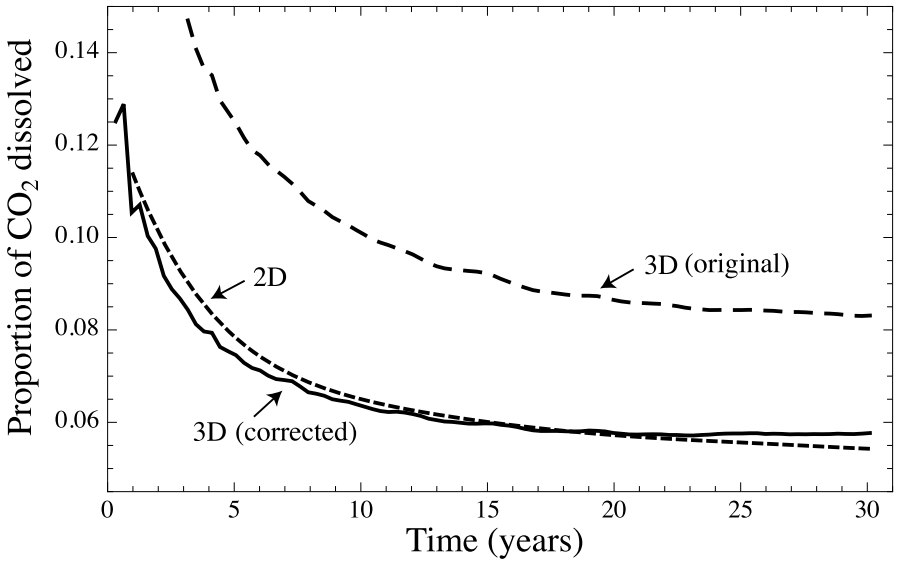

Figure 3.2: Proportion of injected CO_2 dissolved: Comparison between original and corrected coarse-scale 3D Cartesian results with fine-scale 2D radial results for the radial injection problem

In Fig. 3.2 it is readily apparent that the correction obtained using the simple scaling result of Eq. (3.2) significantly improves the result from the coarse-scale simulation. In particular, the relative error between the fine-scale 2D results and the corrected coarse-scale 3D results is only approximately 6% after 30 years of injection, compared to more than 50% relative error in the original (uncorrected) results.

This result demonstrates that the correction provided by Eq. (3.2) can be successfully applied to the results of a coarse-scale model so that the calculated dissolved mass fraction better matches fine-scale results. The scaling can also be used in a different manner, which can improve the coarse-scale model results without post-simulation correction.

If the geometry of the plume can be determined prior to simulation through application of a suitable theoretical model (Dentz and Tartakovsky (2009); Nordbotten and Celia (2006); Nordbotten et al. (2005)) or other estimate, then the magnitude of the error in dissolved mass fraction due to the finite grid blocks can be estimated beforehand. This knowledge could then be used to reduce this error by means of a reduced CO_2 solubility.

Having a simple estimate of the magnitude of the overestimation of the proportion of dissolved CO_2 due to the finite size of the computational grid blocks also allows the construction of computational grids which limit this error to an acceptable value. This requires no access to code, no post-simulation correction, and can be undertaken for any simulator. By constraining the size of the grid blocks so that the ratio of the volume of the blocks that exist at the front to the total volume is always less than a specified value, the error in the calculated dissolved mass fraction can be kept below the desired value. For the radial model, the volume of the front to the total volume scales as $2\Delta r/r$, where r is the radial distance and Δr is the width of the grid block at r. If this ratio is kept to a constant value c, then the error in the calculated dissolved CO_2 mass fraction is $1/(1+c)$ from Eq. (3.2). As a result, the magnitude of this error can be kept below a desired threshold. This approach would result in a finer scale mesh near the well, with increasingly coarse blocks as the radial distance increases. This type of mesh is routinely created in practice. However, the scaling presented in Eq. (3.2) can be used to calculate the degree of refinement needed to keep this error below the threshold in a quantitative manner, rather than simple increasing the resolution arbitrarily. This allows the creation

of an optimal grid for this type of problem, effectively minimising the computational cost for a given accuracy in dissolved CO_2 fraction.

This approach can also be applied to other geometries that may be more complicated than the simple radial model considered here, provided an estimate of the plume geometry is available, either through available theoretical models, or by way of simple argument based on reservoir structure and geometry.

The scaling could also be used as part of an adaptive mesh refinement algorithm to ensure that localised refinement of the grid is sufficient to minimise the error in dissolved mass fraction.

Finally, we note that the correction presented in this section is primarily for application to short-term simulations. For long-term results, this finite grid effect is only a secondary source of error. In this regime, the primary error source due to finite grid sizes is the delayed onset of convective mixing, as shall be considered in the following sections.

4 Convective mixing in homogeneous media

We now consider the long-term numerical predictions of CO_2 dissolution, which depend strongly on the accurate characterisation of the convective mixing process. In order to develop a methodology for including this fine-scale process in a field-scale numerical simulation, an understanding of the density-driven convective mixing process is necessary. In particular, theoretical estimates or formulae of the important characteristics of convective mixing are necessary to implement a sub-grid scheme that accounts for this process that occurs on a length scale smaller than can be resolved in a field-scale simulation.

4.1 Governing equations

Convective mixing of dissolved CO_2 in brine is a complex problem described by coupled differential equations. The equations governing this density-driven convective mixing are Darcy's law for fluid flow in a porous media, and the convection-diffusion equation for transport of the dissolved solute. They are commonly expressed as

$$\mathbf{u} = -\frac{k}{\mu}\left(\nabla P - \rho_f g \hat{z}\right), \tag{4.1}$$

and

$$\phi\frac{\partial C}{\partial t} + \mathbf{u}\cdot\nabla C = \phi D\nabla^2 C, \tag{4.2}$$

where $\mathbf{u}$ is the Darcy velocity, k is permeability, μ is the fluid viscosity, P is the pressure, ρ_f is the fluid density, g is the acceleration due to gravity, $\hat{z}$ is the unit vector in the direction of gravity, ϕ is the porosity of the porous medium, C is the solute concentration, t is time, and D is the diffusion coefficient, the product of diffusivity and tortuosity (Ennis-King et al., 2005). The fluid is also assumed to be incompressible, so

$$\nabla\cdot\mathbf{u} = 0. \tag{4.3}$$

The coupling between Eqs. (4.1) and (4.2) arises due to the effect on fluid density of the concentration of solute, which is given by

$$\rho_f = \rho_0\left(1 + \frac{\Delta\rho}{\rho_0 C_0}C\right), \tag{4.4}$$

where ρ_0 is the density of the unsaturated fluid, C_0 is the maximum solute concentration, and $\Delta\rho = \rho - \rho_0$ is the maximum density increase with concentration. In the following, it will be assumed that $\Delta\rho > 0$, i.e., that increased solute concentration increases fluid density. This assumption is appropriate for dissolved CO_2.

To simplify the analysis, it is commonly assumed that the dependence of ρ_f on C is only retained in the buoyancy term in Eq. (4.1), effectively linearising the dependence of density to concentration. This approximation, known as the Boussinesq approximation (Bear, 1972), is appropriate for CO_2 dissolved in brine due to the weak dependence of partial molar volume on concentration (Ennis-King et al., 2005).

The governing equations are completed with appropriate boundary and initial conditions. If the porous media is considered an infinitely long horizontal reservoir of fixed height H, see Figure 2.1, the boundary conditions at the top ($z = 0$) and bottom ($z = H$) surfaces are given by

$$w(x,0,t) = 0, \qquad w(x,H,t) = 0, \tag{4.5}$$

$$C(x,0,t) = C_0, \qquad \left.\frac{\partial C(x,z,t)}{\partial z}\right|_{z=H} = 0, \tag{4.6}$$

respectively, where C_0 is the solubility of CO_2 in brine. The physical significance of these boundary conditions are to represent a fixed concentration at the upper surface, and a no-flux boundary at

the base of the reservoir. The presence of a fixed concentration boundary at the upper surface is supported by the numerical simulation studies of Lindeberg and Bergmo (2003), Ennis-King and Paterson (2003), and Ennis-King and Paterson (2005), where it was observed that the interface between the gaseous CO_2 and brine remains sharp despite the presence of fingers of CO_2 saturated brine sinking into the less dense unsaturated brine. In reality, this assumption is a simplification of the true interface at the boundary layer, where two phase flow exists.

The initial conditions are

$$\mathbf{u}(x, z, 0) = 0, \qquad C(x, z, 0) = 0 \,\text{for}\, z > 0, \tag{4.7}$$

which correspond to no initial velocity and zero initial solute concentration in the reservoir (apart from the top boundary).

Significant insight into the importance of various processes and properties can be obtained by non-dimensionalising the governing equations. For the case of the horizontal reservoir considered in Figure 2.1, several choices of scaling are obvious. Concentration C is scaled by C_0, and all lengths are scaled by the reservoir height H. Typical diffusive scales are employed for time and velocity. Velocities are therefore scaled by $\phi D/H$, and time is scaled by H^2/D. Pressure is scaled by $\phi\mu D/k$. The governing equations, boundary conditions and initial conditions become

$$\mathbf{u}^* = -\nabla P^* + RaC^*\hat{z}, \tag{4.8}$$

$$\frac{\partial C^*}{\partial t^*} + \mathbf{u}^* \cdot \nabla C^* = \nabla^2 C^*, \tag{4.9}$$

$$w^*(x^*, 0, t^*) = 0, \qquad w^*(x^*, 1, t^*) = 0, \tag{4.10}$$

$$C^*(x^*, 0, t^*) = 1, \qquad \left.\frac{\partial C^*(x^*, z^*, t^*)}{\partial z^*}\right|_{z^*=1} = 0, \tag{4.11}$$

$$\mathbf{u}^*(x^*, z^*, 0) = 0, \qquad C^*(x^*, z^*, 0) = 0 \,\text{for}\, z^* > 0, \tag{4.12}$$

where the superscript asterisk denotes a dimensionless variable, and Ra is the Rayleigh number, given by

$$Ra = \frac{k\Delta\rho g C_0 H}{\phi\mu D}. \tag{4.13}$$

This dimensionless number is a measure of the relative importance of density-driven convection to purely diffusive motion. When Ra is large, convection may occur.

4.2 Isotropic media

Due to the coupled nature of the equations governing convective mixing in a porous medium, analytical results are limited to a small number of tractable cases featuring simplistic models. The vast majority of these cases concern homogeneous reservoirs.

Most theoretical studies have focussed on estimating the critical time for the onset of convective mixing, the critical wavelength of the fingers that form as the dense CO_2 rich brine mixes into the less dense unsaturated brine, and the rate of mass transfer of CO_2 due to convective mixing. A detailed review of the instability of boundary layers in porous media is presented in Rees et al. (2008), where results from different approaches are compared and evaluated. In most cases, only linear systems are considered.

For an isotropic homogeneous porous media, Ennis-King and Paterson (2003), and Ennis-King and Paterson (2005) used linear stability analysis to estimate the critical time for the onset of convective mixing, t_c, which is given by

$$t_c = c_1 \frac{\phi^2\mu^2 D}{k^2(\Delta\rho)^2 g^2}, \tag{4.14}$$

where c_1 is a constant. Ennis-King and Paterson (2005) calculated $c_1 \approx 78$ for an isotropic, homogenous porous media. Using a similar analysis, Xu et al. (2006) calculated $c_1 = 75.19$.

Riaz et al. (2006) used a different time scale in their analysis of this problem, scaling time with $\phi H^2/D$, and consequently obtained slightly different results for the critical time and the value of the constant. A detailed numerical study by Pau et al. (2010) demonstrated that the choice of scale presented in this article is more appropriate for this problem. Specifically, Pau et al. (2010) demonstrated that t_c varies linearly with ϕ^2 and D, while being inversely proportional to k, and thus verified the functional form of Eq. (4.14).

Slim and Ramakrishnan (2010) extended the theoretical analysis of the critical time for the onset of density-driven convection in a porous medium using linear stability and energy stability techniques. In so doing, they derived critical times for various regimes of Ra. Unlike previous studies that relied on implicit assumptions of when a perturbation occurs, no such assumptions are necessary. Slim and Ramakrishnan (2010) present stability diagrams showing that no convection is possible for $Ra < 32.5$. Above this value of the Rayleigh number, convection is possible with a minimum onset time depending on Ra. For $Ra > 75$, the earliest possible time for the onset of a convective instability is independent of Ra, and is given by Eq. (4.14) but with a constant given by $c_1 = 47.9$. This time is significantly earlier than that estimated by Ennis-King and Paterson (2005) and Xu et al. (2006).

The critical wavelength λ_c of the instability for an isotropic homogeneous porous media can also be calculated in this manner (Ennis-King and Paterson, 2005; Xu et al., 2006)

$$\lambda_c = c_2 \frac{\phi \mu D}{k \Delta \rho g}, \tag{4.15}$$

where c_2 is a constant. Ennis-King and Paterson (2005) calculates $c_2 \approx 92$, while Xu et al. (2006) gives a value of $c_2 = 96.23$.

High resolution numerical simulations have shown that the mass flux oscillates about a constant value in the long term, with temporal variations of the order of 15% (Hesse et al., 2006; Pruess and Zhang, 2008; Pau et al., 2010). It's probable that these fluctuations depend on the size of the simulation domain. For simulations over a much larger lateral domain, with small random variations in permeability (which are needed to seed the instability even in isotropic media) one would expect that the temporal fluctuations would average out quite rapidly after the onset of convection. This could be demonstrated in an approximate way by averaging the dissolution flux across a number of independent realisations of permeability.

The functional form of this long-term mass flux of CO_2 per unit width in a two-dimensional model, F_m, is given by (Hesse et al., 2006; Pau et al., 2010)

$$F_m \approx 0.017 \frac{k C_0 \Delta \rho g}{\mu}, \tag{4.16}$$

where the constant 0.017 is calculated from numerical results. Pau et al. (2010) presented analogous results for three dimensions, observing that the mass flux exhibits similar long-term behaviour as the two-dimensional case.

Neufeld et al. (2010) examined the relationship between the convective mass flux and Ra, and determined through numerical simulations and experimental analogues that the convective mass flux scales as $Ra^{4/5}$, in contrast with the classical linear relationship. Using simple analytical arguments, Neufeld et al. (2010) provided a theoretical basis for their findings. However, the dependence on the reservoir height suggests that this finding is only valid for a regime where the downward flux of CO_2 is influenced by the base of the reservoir.

Elenius and Johannsen (2012) investigated the onset time of the fully nonlinear convective regime, defined by the authors as the time where the dissolution rate shows a rapid increase from the initial diffusive decay. This rapid increase corresponds to the point in time where the convective fingers begin to coalesce. Note that this time is different to the critical time for the onset of convection t_c discussed earlier. Ensemble averages of 300 simulations with various initial perturbations are used to examine the time for the onset of the fully nonlinear regime, where it was observed that this time was more than 30 times larger than t_c. This finding suggests that the onset time for fully nonlinear convection should be used in practical applications such as field-scale simulations.

Values for the critical time for the onset of convection, t_c, the critical wavelength λ_c, and the long-term mass flux of CO_2 due to convective mixing for typical reservoir parameters are presented in Table 4.2. Typical fluid properties are given in Table 4.1.

Table 4.1: Typical fluid properties.

Viscosity, μ	0.5947×10^{-3} (kg m^{-1} s^{-1})
Unsaturated brine density, ρ_0	994 (kg m^{-3})
Saturated brine density, ρ	1004.5 (kg m^{-3})
CO_2 solubility in brine, C_0	49.0 (kg m^{-3})
Diffusion coefficient, D	2×10^{-9} (m^2 s^{-1})

Table 4.2: Critical time for the onset of convection t_c, critical wavelength λ_c, and long-term mass flux F_m. Typical fluid properties presented in Table 4.1.

ϕ	k (md)	t_c (s)	λ_c (m)	F_m (kg m^{-2} s^{-1})
0.1	10	5.2×10^8 (16.5 years)	10.7	1.4×10^{-9}
	100	5.2×10^6 (60 days)	1.1	14.4×10^{-9}
	1000	5.2×10^4 (14 hours)	0.1	144.4×10^{-9}
0.2	10	2.1×10^9 (66.5 years)	21.3	1.4×10^{-9}
	100	2.1×10^7 (243 days)	2.1	14.4×10^{-9}
	1000	2.1×10^5 (2.4 days)	0.2	144.4×10^{-9}
0.3	10	4.7×10^9 (148.9 years)	32.0	1.4×10^{-9}
	100	4.7×10^7 (1.5 years)	3.2	14.4×10^{-9}
	1000	4.7×10^5 (5.4 days)	0.3	144.4×10^{-9}

In these examples, convective mixing can occur at times ranging from less than one year up to over one hundred years, depending on permeability and porosity. The critical wavelength ranges from tens of metres to tens of centimetres, and the long-term steady mass flux varies from 1.4×10^{-9} kg m^{-2} s^{-1} to 144×10^{-9} kg m^{-2} s^{-1}. If the thickness of the CO_2 layer is h and the density of the gas-phase CO_2 is ρ_c then the time needed to dissolve the layer completely is approximately

$$\frac{\phi \rho_c h}{F_m} \tag{4.17}$$

assuming that the time for the onset of convection is short compared to this, and that the flux remains steady until complete dissolution. For $\rho_c = 600$kg m^{-3}, $\phi = 0.2$, and $h = 1$m, a flux of 1.4×10^{-9} kg m^{-2} s^{-1} corresponds to a dissolution time of 2700 years, while a flux of 144×10^{-9} kg m^{-2} s^{-1} corresponds to a dissolution time of 27 years.

These values suggest that convective mixing can occur relatively quickly in comparison to the total simulated life of a project, which may be thousands of years, especially for higher permeabilities. Importantly, the critical wavelength, which can be on the cm scale, is typically orders of magnitude smaller than the lateral dimensions of numerical grid blocks used in field-scale simulations. As a result, field-scale simulations do not properly account for the increased dissolution rate due to convective mixing.

4.3 Anisotropic media

Analysis of the critical time and critical wavelength of density-driven convective mixing has been extended to the case of anisotropic homogeneous porous media by several authors. Expressions for t_c and λ_c have been extended to the case of anisotropic homogenous media by Ennis-King et al. (2005); Ennis-King and Paterson (2005); Xu et al. (2006) and Cheng et al. (2012). When anisotropy is included, the constants c_1 and c_2 in Eqs. (4.14) and (4.15) become functions of $\gamma = k_v/k_h$, where k_v and k_h are the permeabilities in the vertical and horizontal directions, respectively. The values of these coefficients are summarised in Table 4.3 for a scaling where the permeability in Eqs. (4.14) and (4.15) is replaced with the horizontal permeability k_h. The result for $c_2(\gamma)$ calculated by Ennis-King et al. (2005) is corrected by including a factor of $\gamma^{-0.5}$ that was omitted in Ennis-King et al. (2005). The scaling used by Xu et al. (2006) and Cheng et al. (2012) to calculate the coefficients $c_1(\gamma)$ and $c_2(\gamma)$ is modified so that the horizontal permeability is used to scale the expressions for t_c and λ_c given by Eqs. (4.14) and (4.15), respectively, for consistency with the results of Ennis-King et al. (2005). Reasonable agreement between the dependence of $c_1(\gamma)$ and $c_2(\gamma)$ on the anisotropy parameter γ is observed in all three cases, see Table 4.3.

Table 4.3: Coefficients $c_1(\gamma)$ and $c_2(\gamma)$ for the critical time and critical wavelength estimates for anisotropic media, respectively. [1] The result for $c_2(\gamma)$ corrects the value given in Ennis-King et al. (2005) where a factor of $\gamma^{-0.5}$ was omitted. [2] The permeability scaling used in Xu et al. (2006) is changed to k_h for consistency with Ennis-King et al. (2005). [3] The permeability scaling used in Cheng et al. (2012) is changed to k_h for consistency with Ennis-King et al. (2005).

	$c_1(\gamma)$	$c_2(\gamma)$
Ennis-King et al. (2005) [1]	$75\,\gamma^{-1.16}$	$95\,\gamma^{-0.758}$
Xu et al. (2006) [2]	$75.19\,\gamma^{-1.258}$	$96.23\,\gamma^{-0.849}$
Cheng et al. (2012) [3]	$47.9\,\gamma^{-1.21}$	$115.3\,\gamma^{-0.83}$

However, to date, no estimate of the long-term average mass flux for anisotropic porous media has appeared in the literature to the best of our knowledge, despite its significance to geological storage of CO_2.

Following Neufeld et al. (2010), we use a simple scaling analysis to determine the functional dependence of the estimate for the long-term average mass flux on the anisotropy of a two-dimensional reservoir. The physical description consists of downward moving plumes of CO_2-rich formation water adjacent to upwelling plumes of fresh water. These upwelling plumes reach the top of the reservoir, and are forced laterally into a mixing region in a flow which behaves like a stagnation flow (Neufeld et al., 2010). The lateral flow in the mixing region acts to stabilise the diffusive boundary layer, which has thickness $\delta = (Dl/u)^{1/2}$, where l is the width of the upwelling plume, and u is the lateral fluid velocity in the mixing region.

In the isotropic case, the lateral fluid velocity is equal to the vertical velocity of fluid in the upwelling plume (Neufeld et al., 2010). For the anisotropic case, however, conservation of mass dictates that the ratio of the thickness of the horizontal mixing region to the width of the upwelling plume is equal to γ. This implies that ratio of the lateral fluid velocity in the mixing region to the vertical fluid

velocity in the upwelling plume scales as γ^{-1}. To first order, it is reasonable to assume that the width of the upwelling plume is inversely proportional to k_v (e.g., from the scaling of λ_c with γ from Ennis-King et al. (2005); Ennis-King and Paterson (2005); Xu et al. (2006)). Vertical velocity in the upwelling plumes scales as k_v. It then follows that the flux across the boundary layer, $F_{bl} \sim \phi D \Delta\rho / \delta$, which is equal to the total flux into the reservoir, scales as $(k_v k_h)^{1/2}$, and not k as for an isotropic reservoir.

This suggests that the appropriate permeability to use in the estimate of the average of the long-term mass flux is the geometric mean of the vertical and horizontal permeabilities. The average long-term mass flux for a two-dimensional anisotropic porous media can then be written as

$$F_m(\gamma) \approx 0.017\, \gamma^{1/2}\, \frac{k_h C_0 \Delta\rho g}{\mu}, \tag{4.18}$$

i.e., Eq. (4.16) scaled by $\gamma^{1/2}$ and replacing k with k_h. The accuracy of this formulation will be assessed through a series of detailed numerical simulations in the following section.

5 Convective mixing in heterogeneous media

In contrast to homogeneous reservoirs, comparatively little work on understanding convective mixing in heterogeneous porous media is present in the literature. In particular, theoretical estimates of useful quantities such as the critical time for the onset of convection, the critical wavelength and even the critical value of Ra are lacking. Only a limited number of numerical studies of the effects of heterogeneity on the characteristics of convection have been undertaken, with these providing few broadly applicable observations (Green and Ennis-King, 2010a; Farajzadeh et al., 2011; Lindeberg and Wessel-Berg, 2011; Taheri et al., 2012; Ranganathan et al., 2012; Elenius and Gasda, 2012).

Some inspiration for theoretical analysis may possibly be drawn from studies concerning thermal convection in heterogeneous porous media (Nield and Kuznetsov, 2007; Nield and Simmons, 2007; Simmons et al., 2010). For example, Nield and Simmons (2007) presented an approximate criterion for the establishment of convection in a heterogeneous porous medium.

Studies involving reservoir heterogeneity are usually limited to a simplified but representative form of heterogeneity. One model of heterogeneity that has been applied in practice is a simple model containing thin, horizontal flow barriers in a homogenous medium (Begg and King, 1985; Green and Ennis-King, 2010b; Hesse and Woods, 2010; Lindeberg and Wessel-Berg, 2011; Taheri et al., 2012; Elenius and Gasda, 2012; Green and Ennis-King, 2013). This formulation is relatively simple to implement in numerical simulations, and provides a reservoir where the vertical permeability is significantly smaller than the horizontal permeability, as is often observed in actual reservoirs.

Green and Ennis-King (2010a) presented detailed numerical simulations of convective mixing in a porous medium containing a random distribution of lateral flow barriers in an otherwise homogenous medium to represent vertical heterogeneity. These results demonstrated that convective mixing could occur much earlier in a heterogeneous media than in an upscaled homogeneous model with the same effective vertical permeability. If the characteristic length scale of the convection fingers at the onset of mixing were much smaller than the vertical separation between flow barriers, then the local vertical permeability was controlling parameter. This finding highlighted that heterogeneity on multiple length scales will be important as convection fingers grow, which has obvious implications for upscaling from high-resolution simulations to field-scale simulations. However, Green and Ennis-King (2010a) also observed that the long-term dissolution rate in a heterogeneous model was well-approximated by a homogeneous model with an equivalent effective vertical permeability. Similar observations are made by Lindeberg and Wessel-Berg (2011) for both regularly positioned and randomly distributed horizontal barriers.

Elenius and Gasda (2012) used a regular distribution of horizontal flow barriers to examine their influence on the dissolution rate of CO_2. By considering models with barriers of various lengths, Elenius and Gasda (2012) observed that the presence of barriers reduces the long-term stable mass flux in comparison to the case with no barriers, with the effect being more pronounced with increasing barrier length. Furthermore, Elenius and Gasda (2012) noted that as the barrier length was increased, the temporal growth in the vertical extent of the fingers decreased markedly.

A detailed numerical study of the influence the degree of spatial heterogeneity in permeability has on the character of density-driven dissolution rate of CO_2 in saline aquifers was presented by Farajzadeh et al. (2011). Using a spectral method to generate multiple realisations of permeability heterogeneity of various degree with the same high Rayleigh number, they observed three marked regimes characterised by the Dykstra-Parson coefficient, a measure of the extent of the heterogeneity. For small values of the Dykstra-Parsons coefficient, corresponding to a weakly heterogeneous permeability field, fingering analogous to the homogeneous case was observed, and this regime was termed the heterogeneous fingering regime. In comparison to the homogeneous case, however, the amount of CO_2 dissolved in the heterogeneous case was found to be greater in most instances.

For medium values of the Dykstra-Parsons coefficient, representative of a moderate degree of heterogeneity, significant flux through some pathways of relatively higher local permeability was observed in most cases. This resulted in plumes dominated by the distribution of permeability. As a result, Farajzadeh et al. (2011) termed this the channeling regime. As for the heterogeneous fingering regime, the dissolution rate was typically greater than for the homogenous case.

Finally, for large Dykstra-Parsons coefficients, where heterogeneity is significant, the dissolution rate increased as the square root of time, suggesting that this regime could be adequately represented by a purely dispersive model with an appropriate diffusion coefficient. No fingering was observed.

The work of Farajzadeh et al. (2011) was extended by Ranganathan et al. (2012) to study the effect of the Rayleigh number on the characteristic of density-driven dissolution of CO_2 in saline aquifers. Using a Sequential Gaussian Simulation method to construct heterogeneous permeability fields, they also observed three possible characteristic regimes from plots of the vertical mixing length (an arbitrary length defined by the authors as the vertical distance from the top boundary to the location where the concentration of CO_2 is 10% of its solubility) versus time. Depending on the value of Rayleigh number, the mass transfer of CO_2 is either dominated by diffusion, convective mixing, or features a mixing length growth slower than convection but nearly equal to the diffusive case. However, when the degree of permeability variation is significant, no diffusion-dominated regime is observed, and only two characteristic regimes are possible.

As expected, large-scale permeability heterogeneity can have a significant impact on the onset, rate and characteristic behaviour of convective mixing of CO_2 in saline aquifers. The effects of small-scale heterogeneity, such as that associated with the spatial variation of the pore size distribution, has also been observed to effect the rate of dissolution. Aggelopoulos and Tsakiroglou (2012) presented experimental and numerical results of CO_2 dissolution in columns packed with granular porous media which suggested that while the dissolution rate in this idealised model is relatively unaffected by permeability variation due to the porosity heterogeneity, failing to account for the variation in hydrodynamic dispersion due to the porosity heterogeneity can lead to large discrepancies. It should be noted that the permeability variation considered in this study is small, and that larger permeability heterogeneity may lead to more significant changes to the dissolution rate.

We now consider the effect of heterogeneity on the average long-term mass flux of CO_2 in a saline aquifer. Multiple numerical simulations of heterogeneous media constructed of a random distribution of impermeable barriers were undertaken, with the results suggesting that an anisotropic homogeneous porous media with equivalent bulk vertical permeability provides an adequate approximation of the long-term mass flux in all cases. In contrast, the critical time for the onset of convection is significantly delayed in the anisotropic model in comparison to the heterogeneous case. In fact, the presence of the impermeable barriers in the heterogeneous case may upset the local equilibrium sufficiently to amplify the convective instability, resulting in a critical onset time that is earlier than even the isotropic homogeneous case.

5.1 Numerical results

Numerical results of the convective mixing process in both anisotropic porous media and heterogeneous porous media are now presented using the TOUGH2 simulator (Pruess et al., 1999). Following Pruess and Zhang (2008), we use the EOS7 fluid property module to significantly reduce the computational requirements. In this representation, it is assumed that the system is limited to a single aqueous phase. The density increase due to CO_2 dissolution is modelled with brine in a two component mixture of water and brine. Pruess and Zhang (2008) and Pau et al. (2010) demonstrated that excellent agreement between this simplified approach and using the ECO2N fluid property module was achieved with a significant reduction in computational expense.

To further reduce the computational expense, only two-dimensional models were considered. The

computational domain was 25 m in the horizontal direction, and 50 m in the vertical direction to reduce the effect of the lower boundary on the simulation results. The spatial resolution was 0.1 m in both the vertical and horizontal directions.

Fluid and reservoir properties used in all simulations are summarised in Table 5.1.

Table 5.1: Parameters used in this study.

Pressure, P	11.4 MPa
Temperature, T	59°C
Porosity, ϕ	0.25
Horizontal permeability, k_h	4.44×10^{-13} m^2 (450 md)
Viscosity, μ	0.485×10^{-3} kg m^{-1} s^{-1}
Unsaturated brine density, ρ_0	994.8 kg m^{-3}
Saturated brine density, ρ	1004.7 kg m^{-3}
CO_2 solubility in brine, C_0	44.0 kg m^{-3}
Diffusion coefficient, D	2×10^{-9} m^2 s^{-1}

The top boundary of the model was kept at a constant saturated concentration, while the bottom was modelled as a no flow boundary. Periodic boundary conditions were imposed along the lateral boundaries. Simulations were run for a time sufficient to obtain a steady long-term mass flux,

Heterogeneity was examined using a simplified model consisting of impermeable horizontal barriers of a specified average length randomly distributed throughout an otherwise homogeneous reservoir at a specified volume fraction. This model of heterogeneity has been used by the authors previously in studies of CO_2 storage in heterogeneous reservoirs (Green and Ennis-King, 2010b,a, 2013), while other studies using regular or randomly distributed barriers to create heterogeneity for CO_2 storage have also appeared in the literature (Hesse and Woods, 2010; Lindeberg and Wessel-Berg, 2011; Taheri et al., 2012; Elenius and Gasda, 2012). In terms of the present study, this simple model of heterogeneity is attractive as it enables the vertical permeability to be reduced while having a small effect on the horizontal permeability. The results of the heterogeneous simulations can then be readily compared against the results for the anisotropic cases with identical effective γ. In these comparisons, the spatial grid resolution for the anisotropic and heterogeneous cases of equivalent anisotropy were identical to limit numerical discrepancies.

Three barrier lengths were considered in this study: short barriers of average length $\bar{L} = 0.1$ m; medium barriers of average length $\bar{L} = 1$ m; and long barriers of average length $\bar{L} = 5$ m. The short barriers were much smaller than the average wavelength of the fingers, the medium barriers were of the same order as the finger wavelength, while the long barriers were typically much longer than the finger wavelength. Heterogeneous realisations with similar effective vertical permeability can be generated using each barrier length with various volume fractions, so that the effect of barrier size can be evaluated.

An example of the dissolved mass fraction for two heterogeneous cases are presented in Figure 5.1. In both cases, the effective vertical permeability is reduced to only 60% of the horizontal permeability ($\gamma = 0.6$) due to the presence of the barriers. The heterogeneity in Figure 5.1(a) is provided by short barriers ($\bar{L} = 0.1$ m, while Figure 5.1(b) has longer barriers with $\bar{L} = 1.0$ m. For the case of the short barriers, the geometry of convective fingers are relatively unaffected by the presence of the barriers. This is expected, as the average barrier length is smaller than the expected finger wavelength. For the medium barriers, which are of a similar size to the finger wavelength, a dramatic influence on the shape and location of the convective fingers can be observed. Despite this, the distance that the fingers have travelled is of similar magnitude in each case.

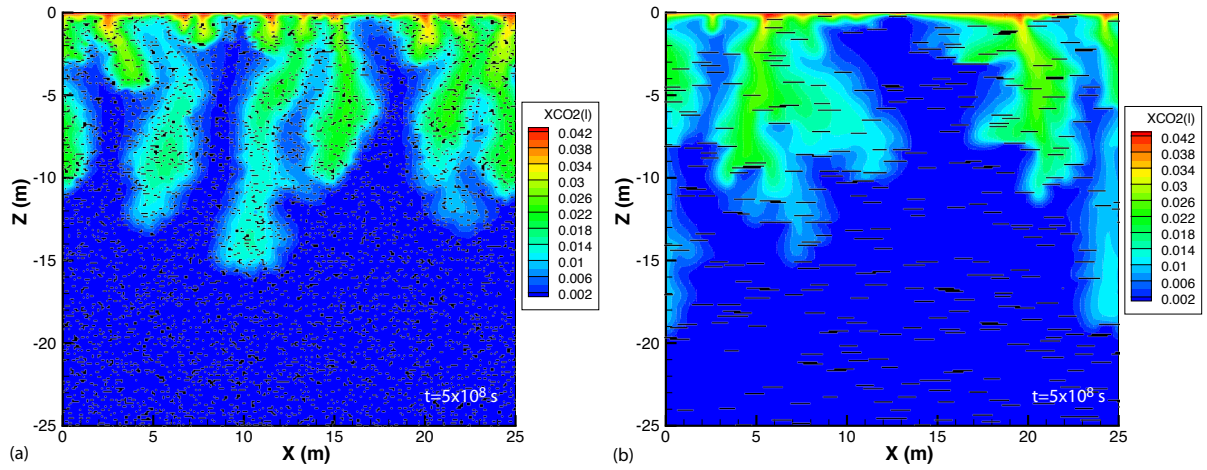

Figure 5.1: Dissolved CO_2 mass fraction for heterogeneous models with $\gamma = 0.6$ after 5×10^8 s (15.8 years). (a) Short barriers ($\bar{L} = 0.1$ m, barriers are shown in black); (b) Medium barriers ($\bar{L} = 1.0$ m, barriers are shown in black).

We now demonstrate that the long-term characteristics of the convective mixing process in heterogeneous media is well approximated by an anisotropic homogeneous model with an equivalent vertical permeability. Numerical simulations of anisotropic porous media for various values of γ were undertaken. To examine the effects of anisotropy on the characteristics of the convective mixing process, the vertical permeability was varied while keeping the horizontal permeability fixed, so that $0 < \gamma \leq 1$.

The computational domain for these anisotropic homogeneous simulations was varied to ensure that more than ten fingers are initially represented (at later times, fingers can merge as they grow larger). Typical ranges for the width of the computational domain varied from 25 m wide for the base isotropic case ($\gamma = 1$), to 75 m wide for $\gamma = 0.05$. The height of the model was typically twice the width. This was sufficient to prevent the convective fingers from reaching the bottom of the model during the simulations. The spatial resolution was typically 0.1 m in the lateral direction, and varied from 1 mm in the vertical direction at the top of the domain to 0.2 m near the base of the model.

An example of the results for a heterogeneous model with an equivalent anisotropic homogeneous model are presented in Figure 5.2. Figure 5.2(a) presents a snapshot of the dissolved mass fraction for a single heterogeneous model with short barriers, where the effective vertical permeability is calculated to be 60% of the horizontal permeability, so that $\gamma = 0.6$. Compared to the dissolved mass fraction of an anisotropic case with $\gamma = 0.6$, we observe that the two models feature a similar number of long convective fingers of similar sizes, suggesting that the anisotropic model may be an adequate representation of the heterogeneous model.

To quantify the comparison between the heterogenous results and those from the equivalent anisotropic case, the mass flux across the top boundary of the simulation domain for each case is compared in Figure 5.3 for the same results presented in Figure 5.2. These results demonstrate that the average long-term mass flux is similar for both the heterogeneous case and the equivalent anisotropic case. However, the anisotropic case significantly delays the onset of convection in comparison to the heterogeneous case. These observations have previously been made by Green and Ennis-King (2010a). Similar results are found for other cases of heterogeneity considered, where the average long-term mass flux from the equivalent anisotropic case is a good representation for the heterogeneous cases but the onset time for convective mixing in the anisotropic model is significantly longer than in the heterogeneous case.

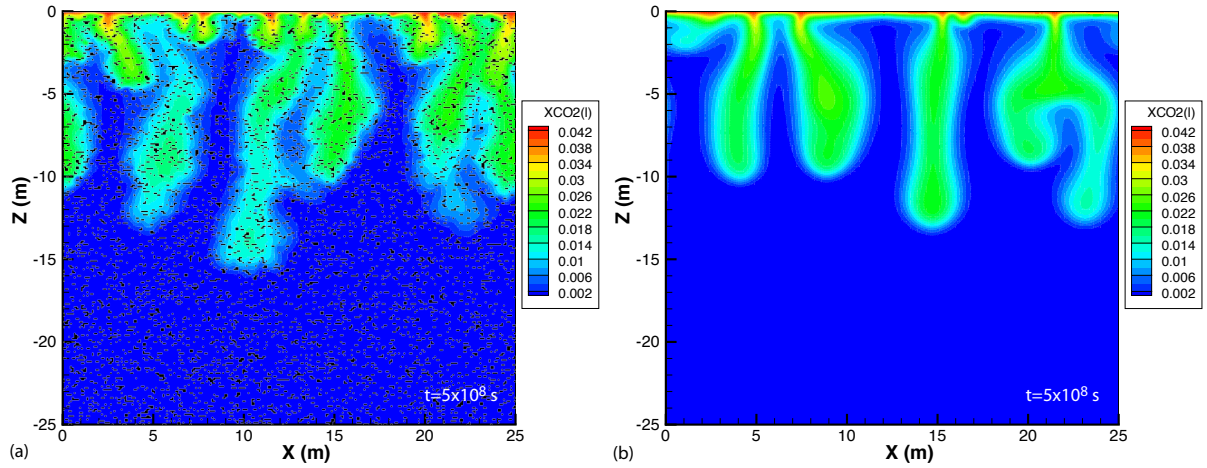

Figure 5.2: Dissolved CO_2 mass fraction for $\gamma = 0.6$ after 5×10^8 s (15.8 years). (a) Heterogeneous case with $\bar{L} = 0.1$ m (barriers are shown in black); (b) Anisotropic homogeneous case.

We now compare the numerical results for $\gamma = 0.05$ to $\gamma = 1$ from anisotropic models as well as heterogeneous representations. The average long-term mass flux for all of these cases is presented in Figure 5.4. Results for an anisotropic model with a higher horizontal permeability of 3.95×10^{-12} m^2 (4 Darcy) are also presented to provide further evidence. Good agreement between all the numerical results and the theoretical scaling of Eq. (4.18) is observed for both anisotropic and heterogeneous cases. The greatest deviation from the theoretical model is observed for the anisotropic cases with the smallest values of γ, which may be the result of numerical effects due to increasing the size of the computational domain for these cases while retaining sufficient spatial refinement. Pruess and Zhang (2008) observed that discretisation errors could arise if the grid is not sufficiently refined, as expected, but also in cases where the grid is too fine. They attributed this surprising result to the possibility of the fine grid impeding the formation and development of fingers of larger wavelength. This is one possibility for the discrepancy in the results for small γ.

For the heterogeneous cases, twenty realisations of each barrier distribution were undertaken, and the mean of the long-term mass fluxes was used in Figure 5.4. The statistical error σ/n, where σ^2 is the variance and n is the number of realisations, is also provided for each case. It is interesting to note that the statistical error is typically small for each value of γ, suggesting that the long-term mass flux is a robust quantity that does not depend greatly on the details of the barrier distribution.

Permeability anisotropy was also observed to increase the onset time for convective mixing, as expected. Results for the onset time for the anisotropic cases are presented in Figure 5.5 as a function of γ. A linear least squares fit to the logarithm of the numerical data suggests that the critical time for the onset of convective mixing scales as $\gamma^{-1.6}$, compared to previously published results of $\gamma^{-1.16}$ (Ennis-King and Paterson, 2005), $\gamma^{-1.258}$ (Xu et al., 2006), and $\gamma^{-1.21}$ (Cheng et al., 2012). The critical time observed in this study is longer than predicted in earlier studies, particularly at small values of γ. This may be attributed to the sensitive dependence of the critical time on the spatial grid resolution observed in numerical simulations (Pruess and Zhang, 2008).

The presence of impermeable barriers was shown to result in much earlier onset times in the heterogeneous case in comparison to the equivalent anisotropic case considered in Figure 5.3. Figure 5.5 clearly demonstrates that the onset time in the heterogeneous model is much earlier than for the equivalent anisotropic case, and typically much earlier than even the homogenous case. We attribute this phenomena to the presence of the impermeable barriers providing a localised disruption to the initial equilibrium in a similar fashion to the initial permeability variation but at a much greater scale.

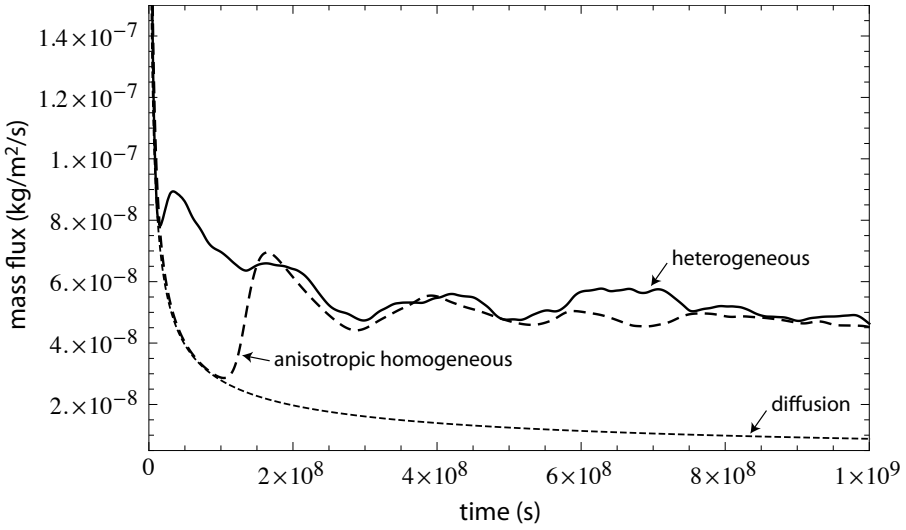

Figure 5.3: Temporal evolution of CO_2 mass flux across the top boundary for $\gamma = 0.6$. Heterogeneous case with $\bar{L} = 0.1$ m (solid line); Anisotropic homogeneous case (long-dashed line). The analytical diffusion solution is also shown (short-dashed line).

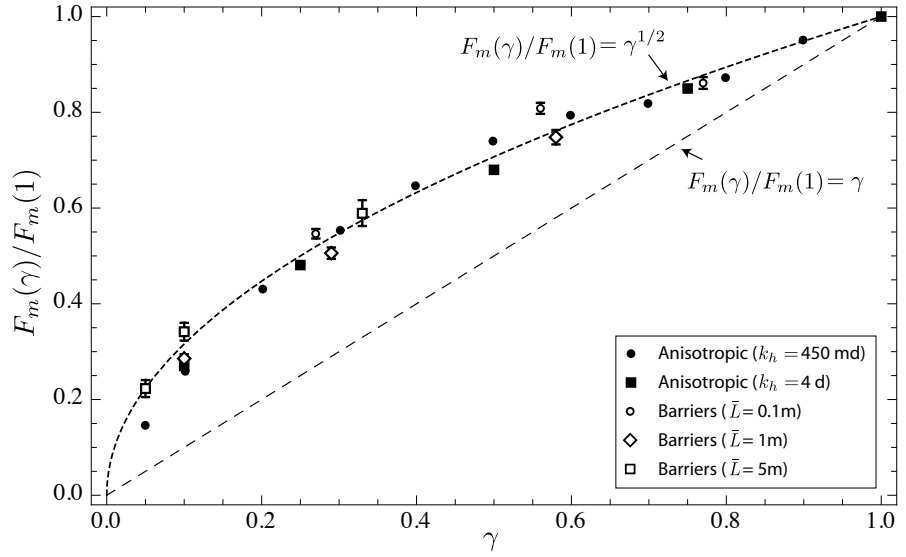

Figure 5.4: Long-term average mass flux $F_m(\gamma)$ scaled by $F_m(1) = 0.017 k_h C_0 \Delta\rho g/\mu$. Simulation results for anisotropic porous medium with $k_h = 450$ md (solid circles); anisotropic porous medium with $k_h = 4$ d (solid squares); heterogeneous media with average barrier length $\bar{L} = 0.1$ m (hollow circles); heterogeneous media with average barrier length $\bar{L} = 1$ m (hollow diamonds); heterogeneous media with average barrier length $\bar{L} = 5$ m (hollow squares). Statistical error $\sigma/\sqrt{n}$ for heterogeneous cases indicated with bars, where σ^2 is the variance and n is the number of realisations. Note in some instances error bars are smaller than the symbol size. Short-dashed line is the analytical model $F_m(\gamma)/F_m(1) = \gamma^{1/2}$. Long-dashed line is $F_m(\gamma)/F_m(1) = \gamma$ for reference.

In contrast to the results for the average long-term mass flux, which closely followed a $\gamma^{1/2}$ scaling with little deviation, significant variance between the onset time for heterogeneous results is observed, even for realisations with different barrier lengths but similar bulk permeabilities. This suggests that the critical onset time may be sensitive to the location and dimensions of the barriers, and not just the average properties.

The theoretical scaling and numerical results presented have been restricted to a simplified two-dimensional model. An identical scaling result could reasonably be expected for an idealised three-dimensional model consisting of arrays of fingers with circular cross sections along the top boundary. However, fine-scale numerical simulations presented by Pau et al. (2010) suggest that the fingering process in the three-dimensional case is extremely complicated, so it remains to be seen whether the anisotropic scaling presented in this study is applicable to three dimensions.

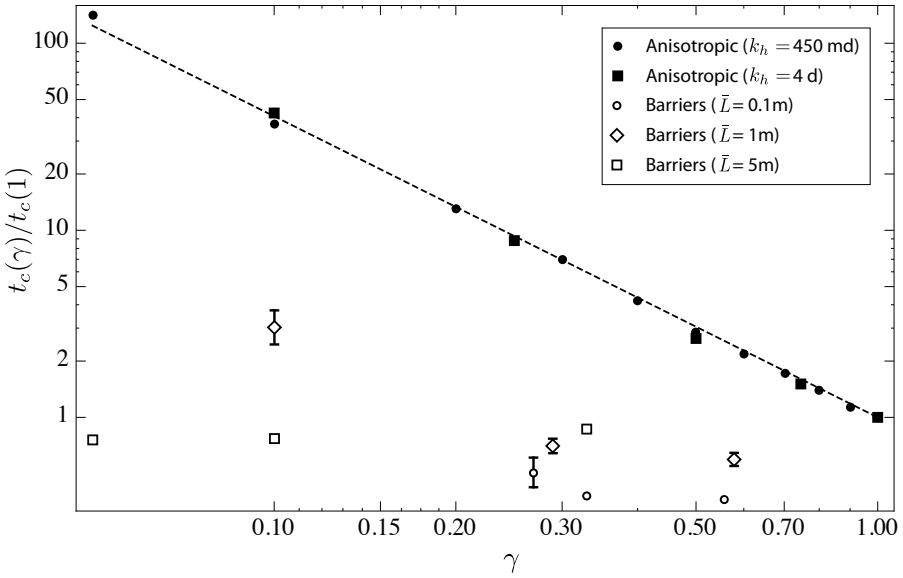

Figure 5.5: Critical time for the onset of convection $t_c(\gamma)$. Simulation results for anisotropic porous medium with $k_h = 450$ md (solid circles); anisotropic porous medium with $k_h = 4$ d (solid squares); heterogeneous media with average barrier length $\bar{L} = 0.1$ m (hollow circles); heterogeneous media with average barrier length $\bar{L} = 1$ m (hollow diamonds); heterogeneous media with average barrier length $\bar{L} = 5$ m (hollow squares). Statistical error $\sigma/\sqrt{n}$ for heterogeneous cases indicated with bars, where σ^2 is the variance and n is the number of realisations. Note in some instances error bars are smaller than the symbol size. Short-dashed line is the best fit to the anisotropic data $t_c(\gamma)/t_c(1) = \gamma^{-1.6}$.

6 Geochemistry

6.1 Background

Another complicating factor that has not received a great deal of attention in the scientific literature is the role of geochemical reactions between the CO_2 and minerals present in the formation during sequestration. While slow reactions with silicate minerals in the reservoir can take hundreds to thousands of years to precipitate a significant fraction of the injected CO_2, reactions with common carbonate minerals such as calcite can occur much faster and influence the onset of convective mixing in the short term.

Ennis-King and Paterson (2007) presented a theoretical and numerical study of the role of geochemistry on the onset and rate of convective mixing of CO_2. If chemical reaction were sufficiently slow, convective mixing could occur as if no reactions were happening, and the geochemical reactions would only play a role in the long-term mineralisation of CO_2. However, when fast acting reactions were considered, significant coupling between the reactions and convective mixing could be expected. First, the reaction could alter the density of the fluid due to changes in solute concentration or even temperature (either exothermic or endothermic). Secondly, reactions between the CO_2 and minerals in the reservoir rock may result in local variations to porosity and permeability. Ennis-King and Paterson (2007) demonstrated using a simple analytical model with a single mineral present that fast-acting chemical reactions can lead to significant increases in the critical time for the onset of convective mixing. Including the effects of geochemical reactions, the critical time could be up to an order of magnitude greater than for the case with no reactions present. However, the wavelength of perturbations remained relatively unchanged.

This effect was considered in detail by Andres and Cardoso (2011), who showed that the density instability with fast chemical reactions was determined solely by the dimensionless parameter

$$\frac{Da}{Ra^2} = \frac{\phi \mu^2 k_r A D}{(k \Delta \rho g)^2}, \tag{6.1}$$

where Da is the dimensionless Damköhler number, which relates the reaction time to the flow transport time, k_r is the kinetic rate constant, and A is the area per unit volume of mineral. For $Da/Ra^2 \lesssim 0.002$, convection can occur, with a critical time to onset that grows linearly with increasing Da/Ra^2. This indicates that as the reactions occur faster (increasing Da at constant Ra), the critical time for the onset of convection is delayed, as observed by Ennis-King and Paterson (2007). For $Da/Ra^2 > 0.002$, chemical reactions are so rapid as to stabilise the diffusive layer at the CO_2-brine interface, and no convection is possible (Andres and Cardoso, 2011). However, these findings are for the simplified case where reactions continue indefinitely, and it is unclear how these results would be modified when reactions are limited by the finite amount of reactants.

Ghesmat et al. (2011b) presented a linear stability analysis of the effect of geochemical reactions on the onset of convective mixing, and confirmed that fast reactions typically stabilise the diffusive layer thus delaying the onset of convection by reducing the density contrast. Interestingly, the rate of trapped CO_2 was shown to increase in these cases, with mineralisation of CO_2 from the dissolved phase occurring at a rate faster than the decrease in convective mixing resulting from the reduced mass of dissolved CO_2.

Numerical simulations showed that including the effects of geochemical reactions could result in a significantly increased dissolution rate (Ennis-King and Paterson, 2007), see Figure 6.1. For instance, including reactions led to an increase of approximately 30% in the proportion of dissolved CO_2 after 100 years, even neglecting the effect on fluid density of the ionic concentration. When the contribution to the fluid density due to local ion concentration is included in the simulation, the dissolution rate increases further, with an additional 25% of the total CO_2 dissolved, see Figure 6.1.

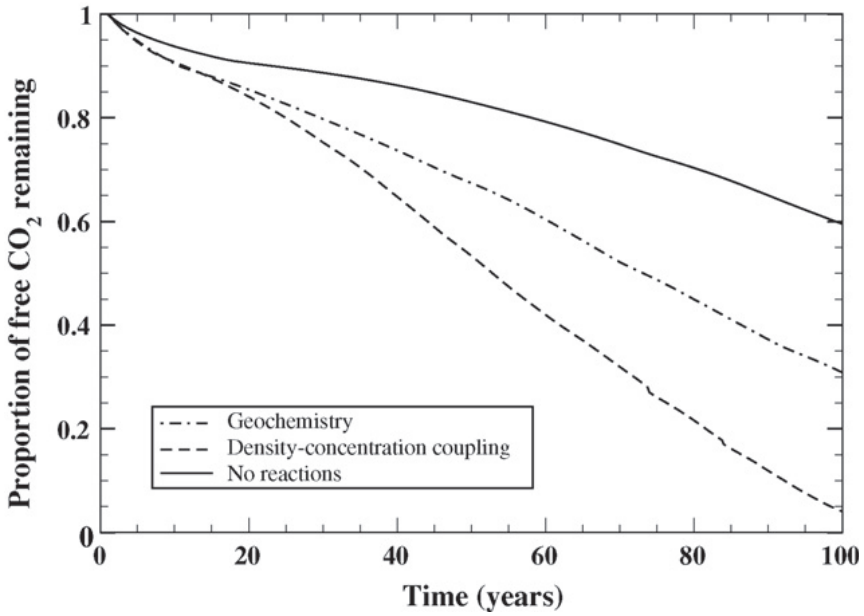

Figure 6.1: Proportion of mobile CO_2 dissolved due to convection for no reactions (solid line); geochemistry included (dotted-dashed line); coupling of ions to fluid density (dashed line). Figures taken from Ennis-King and Paterson (2007).

In the cases considered by Ennis-King and Paterson (2007), decreases in local permeability due to the presence of geochemical reactions were small, and insufficient to impede or inhibit convective mixing. However, it is feasible that some cases of practical interest may feature mineralogy that will enable reactions that will retard convection. Site specific simulations with accurate representations of the mineralogy will therefore be important in obtaining robust predictions.

One of the key findings of Ennis-King and Paterson (2007) that has not received a great deal of attention is that the increase in fluid density due to ion concentration can be of the same order of magnitude as the density increase due to dissolved CO_2. This effect can therefore be an important process in the onset and rate of convective mixing, as confirmed in the sensitivity analysis of Zhang et al. (2011). If this effect is neglected, predictions of the onset time and dissolution rates of convective mixing may vary significantly from their actual values.

6.2 Technical challenges of flux simulation with geochemistry

There are two specific technical challenges that need to be considered in extending the previous simulation work to allow for coupling with geochemical changes. The first challenge is that the computational demands of reactive transport simulation necessitate coarser grids (or longer run times) than for simulations with flow alone. Thus it's important to assess how sensitive the calculation of dissolution flux is to the grid resolution, so that an appropriate resolution can be chosen which allows a direct comparison between convection with geochemistry and convection with flow alone.

The second challenge is how to measure the dissolution flux. The original work in the simulation of density-driven convection had a two-phase region at the top of the system, which allowed for capillary pressure and relative permeability effects in that region, and which enabled one to observe the complete dissolution of the carbon dioxide. The total amount of CO_2 in the simulation is easily tracked, and the numerical derivative of this gives the flux.

In more recent work, flow simulations have employed an effective upper boundary condition (BC) of

constant concentration of dissolved CO_2 in order to model dissolution from a gas phase, while avoiding the need to simulate two-phase effects. This is much more computationally efficient (requiring fewer variables to track per gridblock), although it does not enable one to assess the contributions of the two-phase physics. In practical terms one computes the the dissolution flux into the second row of grid blocks from the top (since the top row is used to impose the constant concentration boundary condition).

When geochemistry is included, there is an extra degree of complication, because the CO_2 may also be mineralised as well as dissolved. One option is to have an explicit two-phase region, and use the decline in the amount of CO_2 in the gas phase to compute the dissolution flux. This is more accurate for the physics of the problem, particularly if the geochemical reactions are affected by the presence of the two-phase region. This is to be expected, since where a gas phase is present in equilibrium with a water phase, the dissolved CO_2 concentration is highest, and reactions often occur to a greater extent than elsewhere. Since reactions may change porosity, this can affect fluid pressures, so in this case it is necessary to have a constant pressure boundary condition along the lower boundary of the simulation domain.

Another option, as discussed above for flow-only simulations, is to use a constant concentration boundary condition, but with no reactions allowed in the top row of gridblocks. The latter is necessary since reactions in the top row of gridblocks (implemented in TOUGHREACT as having large volumes) can have a strong effect on pressure and flow in the small volume gridblocks within the simulation domain. One then computes the diffusive flux into the second top row of gridblocks. This has the virtue of greater simplicity, but at the cost of neglecting the two-phase physics and its possible interaction with the geochemistry. These two options will be explored in the simulation work here.

6.2.1 Grid refinement

To study the effect of grid refinement on the computations of the dissolution flux, first consider a 2D vertical section 25 m wide and 25 m deep with $k_h = 10^{-13}\text{m}^2$ and $k_v/k_h = 0.5$, using an effective boundary condition of constant concentration and no geochemistry. The pressure (at the top) is 20 MPa, and the temperature is 75 C. Fig. 6.2 shows the dissolution fluxes as a function of time at spatial resolutions of 0.1 m, 0.2 m, 0.5 m and 1.0 m. Also shown is the dissolution flux for the 0.5 m resolution but with a two-phase gas region instead of an effective boundary condition. The 0.1 m and 0.2 m resolutions have nearly the same onset time and average long-term flux. The 0.5 m resolution has a later onset time (by about 20 %), but nearly the same average long-term flux. The 1.0 m resolution has a much later onset time (nearly double), the average long-term flux is about 30 % less than the finer resolution cases, and there are no fluctuations in the dissolution flux. The 0.5 m resolution with a two-phase gas region has about the same onset time as the equivalent resolution but with an effective boundary condition. However the long-term average flux is about 20 % lower. It's evident that there is a resolution below which the onset time and the flux are unchanged, as one would expect.

The spatial resolution needed for accurate computation of the flux will depend on the width of fingers at the onset of convection. For example, lower vertical permeability will lead to wider fingers, and so the lateral resolution can be reduced and still give a good estimate of the long-term average flux. Fig. 6.3 shows the dissolution flux as a function of time in a 2D vertical section 75 m wide and 75 m deep with $k_h = 10^{-13}\text{m}^2$ and $k_v/k_h = 0.1$, using an effective boundary condition of constant concentration. In comparison to Fig. 6.2, lowering k_v by a factor of 5 broadens the fingers at onset of convection, so the size of the grid is expanded by a factor of 3 in lateral and vertical dimensions. It is evident that coarser lateral resolutions (0.3 m and 0.6 m) are sufficient to obtain good estimates of the long-term average flux in this case as compared to the previous $k_v/k_h = 0.5$ case.

A more detailed comparison of the impact of the effective boundary condition vs the explicit two-

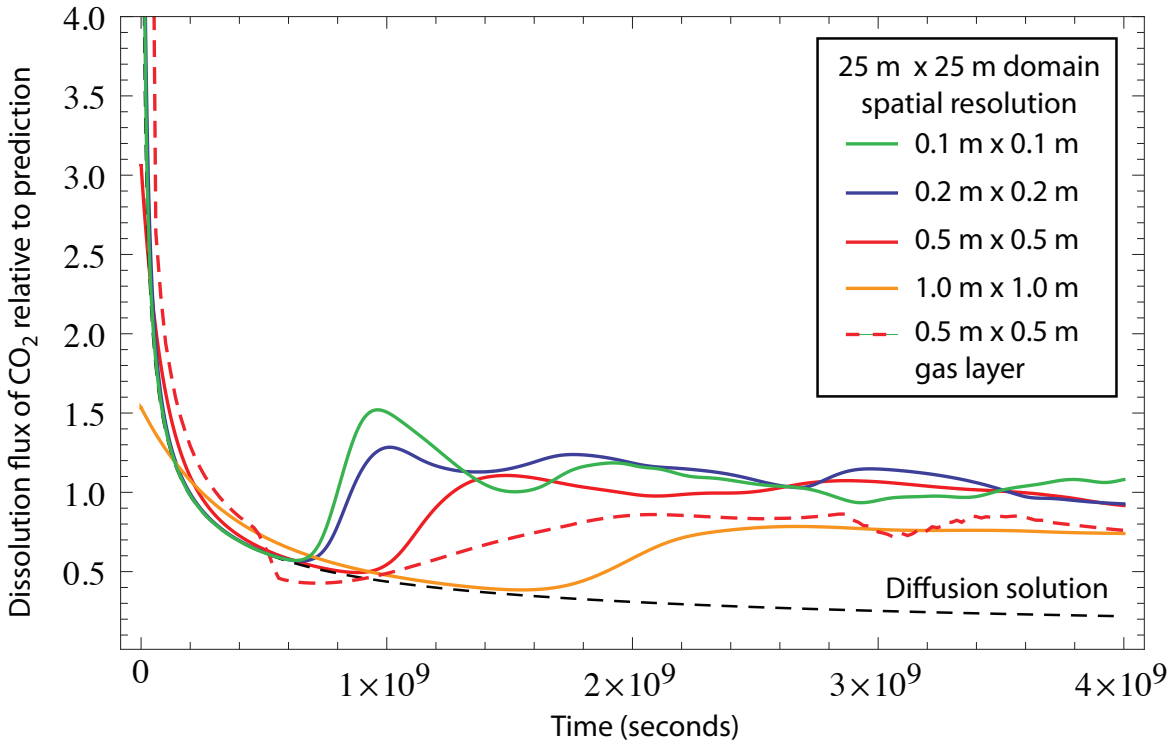

Figure 6.2: Effect of grid refinement on the dissolution flux of CO_2. 2D vertical section, 25 m wide and 25 m deep. $k_h = 10^{-13}\text{m}^2$ and $k_v/k_h = 0.5$. Solid curves: effective BC. Dashes curve: two-phase gas layer.

phase region is shown in Fig. 6.4. The blue curves are for flow without geochemistry, the red curves for flow with geochemistry affected CO_2, and the green curves for flow with geochemistry affecting the fluid density as well. The solid curves use the explicit two-phase region, and the dashed curves are for the effective boundary condition. In the absence of geochemistry, the case with the two-phase region has an earlier onset for convection than the effective boundary conditon case, but the average steady flux is very similar until the gas phase layer is mostly dissolved (around 250-300 years). Once geochemistry is used (affecting CO_2), there is a much earlier onset of convection and a much higher flux (about twice as high) with the explicit gas phase, and larger oscillations in the flux. Most noticeably, the gas phase layer dissolves completely in about 170 years. When the further coupling to ionic density is turned on, then the onset of convection is even earlier, and the flux rises by at least a factor of 3. Then the gas layer dissolves completely in under 110 years.

Now consider the combination of grid refinement with geochemical coupling. This is done on a 25 m by 25 m 2D vertical section. For this a published geochemical model for the Frio formation is used, as employed in Ennis-King and Paterson (2007), combined with the previous parameters of $k_h = 10^{-13}\text{m}^2$ and $k_v/k_h = 0.5$, with a two-phase region rather than an effective boundary condition. Three options are compared:

- flow only (no geochemistry)
- geochemistry which adds or removes CO_2 to/from the flow
- geochemistry which also couples ion concentrations to fluid density

Three grid resolutions are used:

- 50 x 50 blocks (0.5 m x 0.5 m block) (coarse)
- 100 x 100 blocks (0.25m x 0.25 m block) (fine)

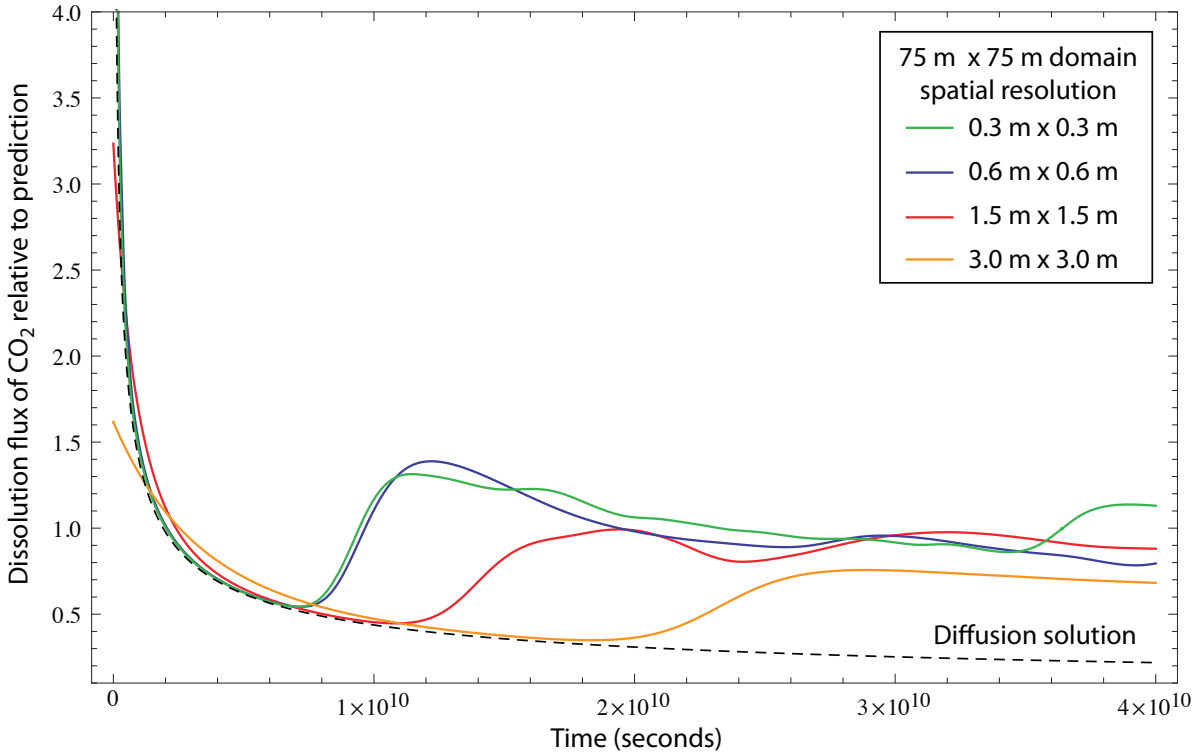

Figure 6.3: Effect of grid refinement on the dissolution flux of CO_2. 2D vertical section, 75 m wide and 75 m deep. $k_h = 10^{-13}\text{m}^2$ and $k_v/k_h = 0.1$. Effective BC of constant concentration at top.

- 200 x 200 blocks (0.125 m x 0.125m block) (vfine)

Fig. 6.5 shows the simulation results for this case. The effects of grid resolution are weak in this range of sizes, with the 0.5 m, 0.25m and 0.125 m grid spacings giving similar average values for the flux and indeed similar fluctuations. The one exception is in the case when geochemistry is coupled to fluid density, and then the fine grid predicts somewhat higher fluxes and more frequent oscillations than the coarse grid. The strongest effect is that of adding geochemistry. Compared to flow alone, the case with geochemistry just adding or removing CO_2 increases the dissolution flux by around 50 %, while including the geochemical coupling to fluid density increases it by a factor of between 2 and 3 in this instance.

6.2.2 Conclusions on technical challenges

As is known from past work, grid resolution affects the timing of the onset of convection, with grids that are coarser than the initial finger spacing delaying the onset of convection. On the other hand, the steady convective flux is relatively insensitive to grid resolution, either with an effective BC or an explicit two-phase region, as long as the grid is finer than the initial finger spacing.

Without geochemistry, the steady flux agrees with the theoretical prediction. With geochemistry, in the case studied the steady flux is 1.5 times the flux in the flow-only case if the consumption of CO_2 is included, and 2-3 times the flow-only average flux if the coupling of reactions to ion density effects is included. Simulations with a two-phase region and geochemistry predict a much higher dissolution flux than the effective BC model, especially with ion density effects included.

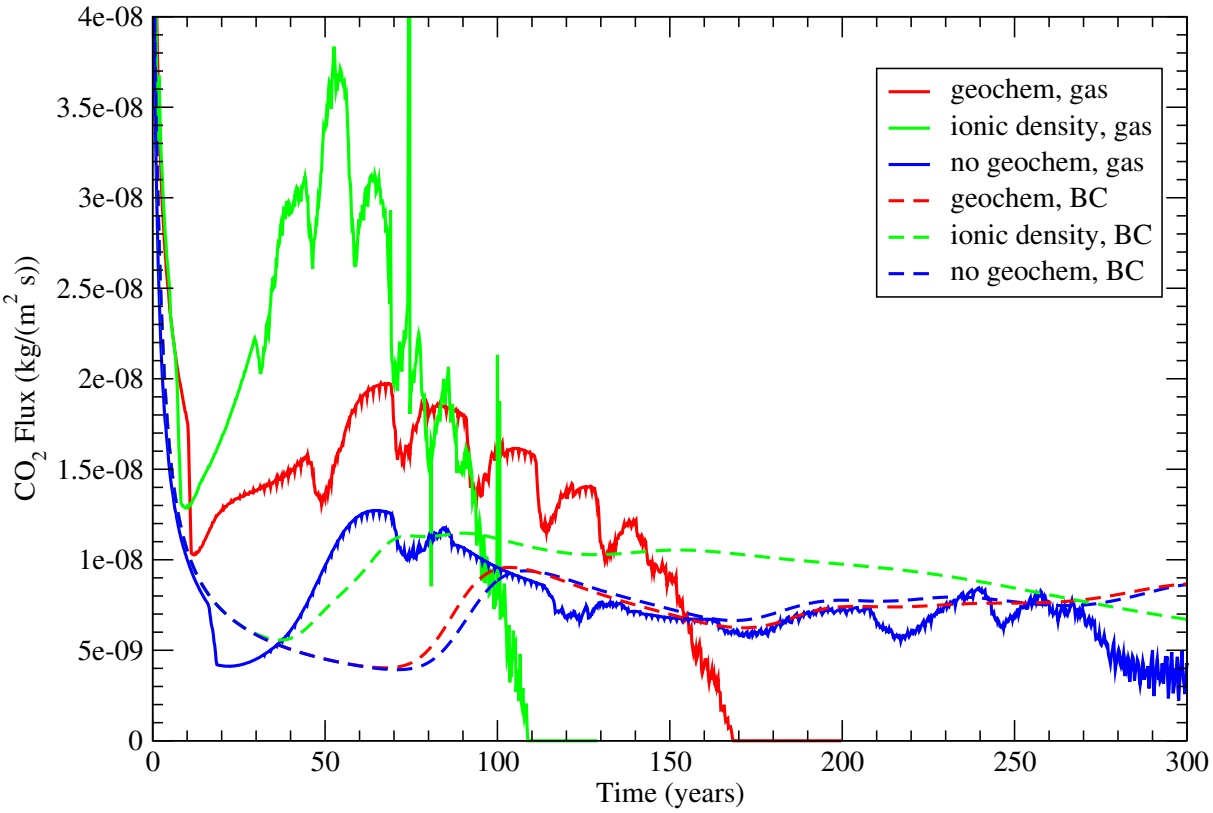

Figure 6.4: Comparison of effective boundary condition and two-phase region on the dissolution flux of CO_2. 2D vertical section, 25 m wide and 25 m deep. $k_h = 10^{-13}\text{m}^2$ and $k_v/k_h = 0.5$.

6.3 Geochemical model for Precipice Sandstone

The geochemical data is taken from the preliminary ANLEC report on the Surat Basin (Haese et al. (2013)). The Precipice Sandstone (sample ID 1190) is quartz-dominated (95.61%), with minor amounts of kaolin (2.46 %), illite (0.95 %), albite (0.59 %), chlorite (0.16 %), anatase (0.10 %), siderite (0.08 %), apatite (0.04 %) and pyrite (0.04 %). In the model, anatase and apatite were omitted based on advice of D. Kirste. Water chemistry is adjusted to be in equilibrium with minerals. In this case the low salinity result (Precipice 1) was used. Reaction path models suggest low reactivity to CO_2, with dissolution of chlorite, albite and illite, and precipitation of kaolinite, siderite and chalcedony.

6.4 Coupling convection and geochemistry in Precipice Sandstone

The geochemical model for the Precipice Sandstone was implemented and equilibrated in TOUGHREACT, at the conditions of interest (11.4 MPa, 59 C). The geometry and permeability of the Frio test system was first used ($k_h = 10^{-13}\text{m}^2$ and $k_v/k_h = 0.5$), to see the effect on convection compared to other geochemical models. Higher permeabilities ($k_h = 4 \times 10^{-12}\text{m}^2$ and $k_v/k_h = 0.5$ or $k_v/k_h = 0.1$), more representative of the Precipice Sandstone, were then tried. Effective boundary condition were used rather than two-phase region, and as shown in the previous section this will underestimate the dissolution flux by around 20 %. Fig. 6.6 shows the case of $k_h = 10^{-13}\text{m}^2$ and $k_v/k_h = 0.5$, comparing the flux with no geochemistry to the cases using the geochemistry of the Frio Sandstone, and the case using the geochemistry of the Precipice Sandstone. With the Frio geochemistry, the onset of convection is sooner than the no geochemistry case, and the average steady

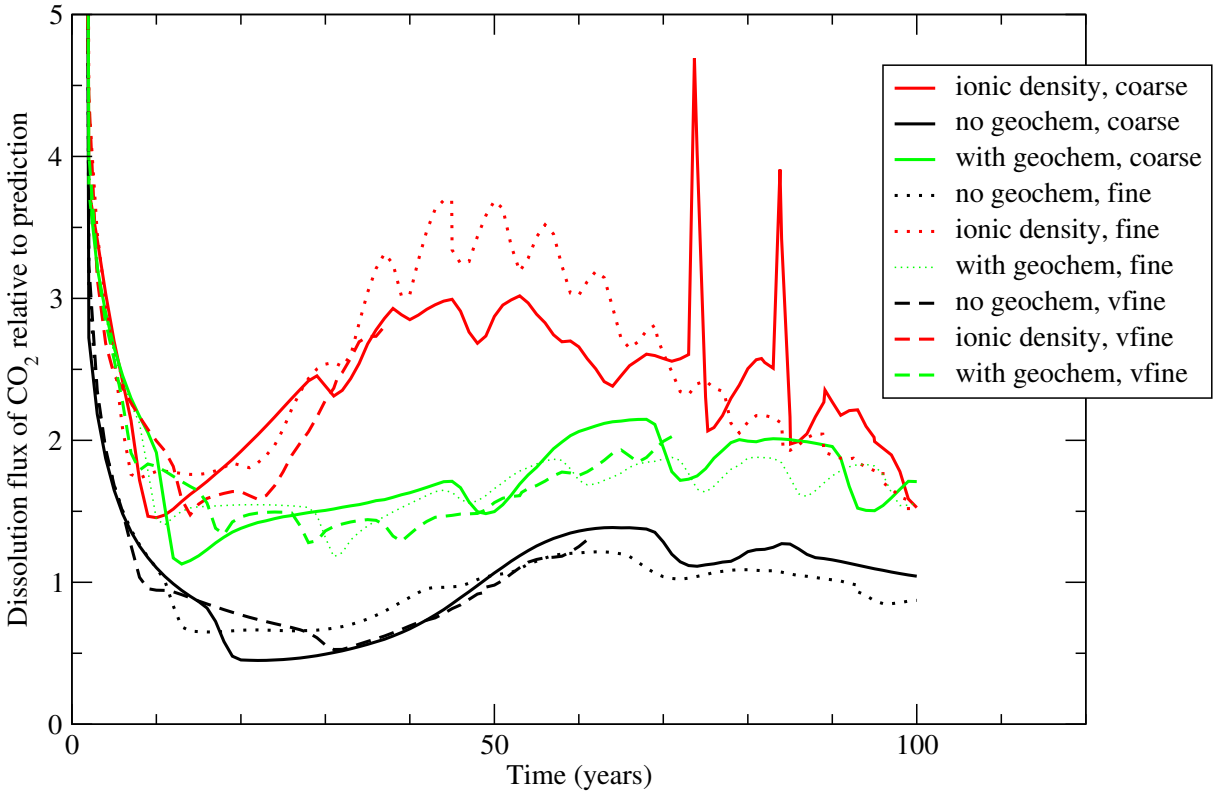

Figure 6.5: Effect of geochemistry and grid refinement on the dissolution flux of CO_2 as a function of time in years. 2D vertical section, 25 m wide and 25 m deep. $k_h = 10^{-13}\text{m}^2$ and $k_v/k_h = 0.5$. The geochemistry is based on a model of the Frio sandstone. There is an explicit two-phase region along the top of the simulation domain.

flux is greater, in line with previous results. Comparing the two different geochemistries, the onset of convection is much later for the Precipice geochemistry (by nearly a factor of two), and the average steady flux looks to be greater (although not enough of the oscillation is seen to be definitive).

Even in a relatively clean sandstone, the inclusion of geochemistry increases the dissolution flux due to convection. Higher permeabilities (horizontal and vertical) increase the dissolution flux, in line with theoretical predictions. Further simulations are needed to explore the effect of a two-phase region on the convective flux with geochemistry, but simulation on the Frio system suggest that the dissolution rate will likely be increased.

The earlier result for effects of anisotropy on convective flux could be modified to take account of geochemical effects. The geochemical coupling contributes most to the density difference term $\Delta\rho$. This could be estimated by a separate geochemical calculation. Preliminary work using simulation indicates that this has the right scaling to explain the flux results. The timing of the onset of convection is also affected by geochemistry, but this is generally a shorter timescale than the dissolution process, and is less important in an upscaled scheme.

6.5 Conclusions for geochemistry

Grid resolution effects on the dissolution flux (with and without geochemistry) are weak once the grid is fine enough to resolve the fingers of dissolved CO_2. Using an explicit two-phase region gives higher fluxes than an effective boundary condition approach, especially when the ion density coupling

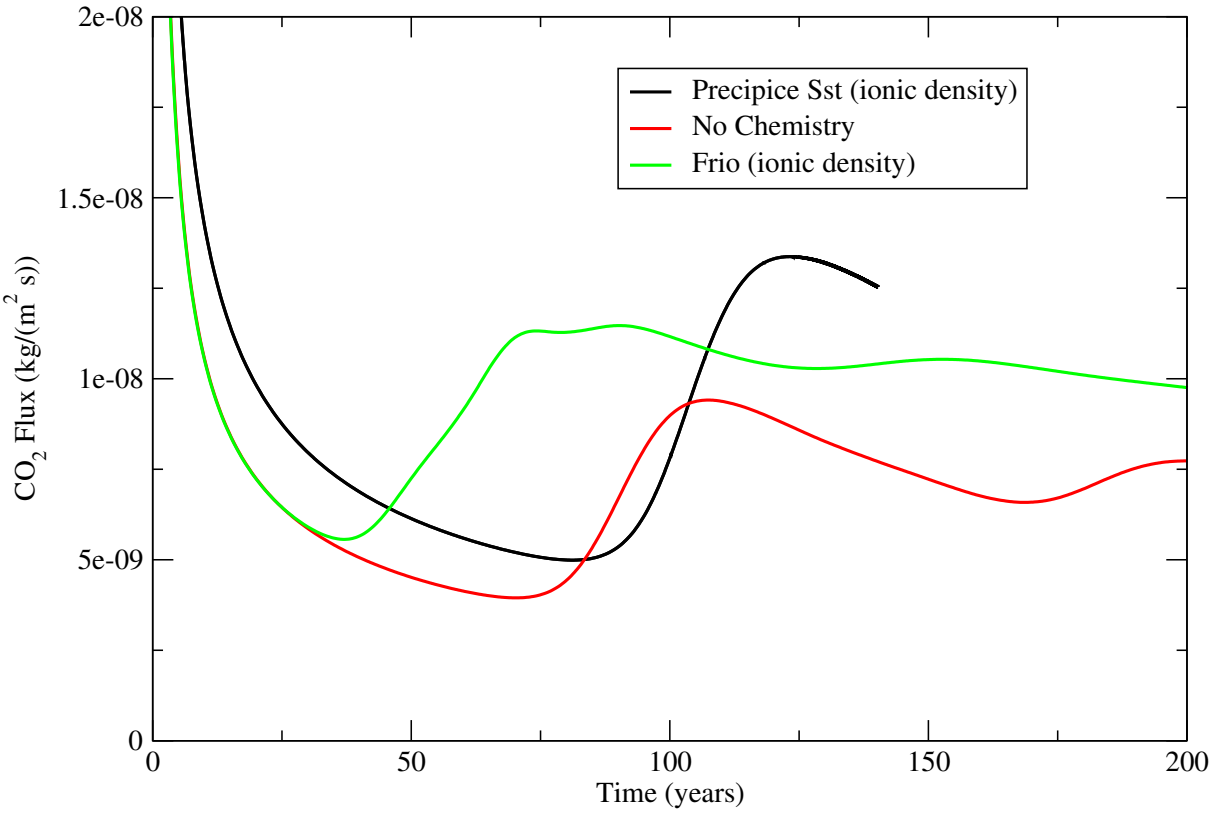

Figure 6.6: Comparison of different geochemical models on the dissolution flux of CO_2 as a function of time in years. 2D vertical section, 25 m wide and 25 m deep. $k_h = 10^{-13}\text{m}^2$ and $k_v/k_h = 0.5$. There is an effective boundary condition of constant concentration along the top of the simulation domain. Red curve: no geochemistry. Black curve: geochemistry from Precipice Sandstone. Green curve from Frio sandstone

is included. Geochemical effects can increase the dissolution flux by a factor of up to 3, especially when the ion density coupling is included.

A geochemical model of the Precipice Sandstone was implemented in TOUGHREACT based on the ANLEC report on the Surat Basin (Haese et al. (2013)). For the Precipice Sandstone, the inclusion of geochemistry increases the dissolution flux due to convection. Higher permeabilities (horizontal and vertical) increase the dissolution flux, in line with theoretical predictions. Further simulations are needed to explore the effect of a two-phase region on the convective flux with geochemistry in the Precipice Sandstone, but simulation on the Frio system suggest that the dissolution rate will likely be increased. Geochemistry could be included in the theoretical expression for the convection flux via the $\Delta\rho$ term. Geochemical effects could thus be incorporated into the upscaled effective dissolution flux.

Current models of CO_2 dissolution omit geochemical effects. For storage in the Precipice Sandstone, this leads to an underestimate of the rate of dissolution and an overestimate of the risk of leakage. Better models (with upscaling of the effects of convection and geochemistry) will reduce the project risk by improving estimates of CO_2 dissolution and long-term storage security.

7 Sub-grid scale model of convective mixing

Thus far, most of the research into convective mixing of CO_2 in a saline aquifer has been concerned with examining simple problems that are analytically tractable, such as estimating the critical time for the onset of convective mixing in a horizontal homogenous reservoir, or with fine-scale simulations with computational domains of the order of metres in width. This is in contrast with field-scale simulations of CO_2 storage, which commonly feature individual grid blocks with dimensions at least one order of magnitude and sometimes two orders of magnitude greater than the total dimensions of these fine-scale models. Consequently, there is a disconnect in length scales between the results concerning convective mixing of CO_2 in saline aquifers currently available in the scientific literature, and the numerical simulations of a practical storage project.

The use of large grid blocks in these studies is necessitated by limits on the available computational power, and the common requirement to perform simulations on a suite of possible geological realisations to mitigate the uncertainty in many important parameters. However, these large grid blocks inhibit the onset of convection within the numerical simulation, and hence underestimate the rate of dissolution. Indeed, when considering the critical wavelength for convective fingers which could be on the centimetre scale (see Table 4.2), it is obvious that grid blocks of lateral dimensions that are several orders of magnitude greater than this will be unable to capture the fingering process accurately.

Comparatively few studies attempting to incorporate fine-scale convective mixing processes into field-scale simulations have been published. Pruess and Nordbotten (2011) included the enhanced dissolution as a result of sub-grid scale convective mixing in a large-scale simulation by way of a rudimentary sink term applied to the region in the uppermost row of grid blocks containing mobile phase CO_2. For the reservoir conditions of the problem considered, the onset time of convective mixing was estimated to be insignificant compared to the total simulation time, and as such, this process was assumed to take place instantaneously.

For a gently sloping reservoir, Pruess and Nordbotten (2011) found that increasing the dissolution rate in this fashion led to a CO_2 plume that was thinner as it migrated updip, while reducing the updip flux. Interestingly, the speed of the plume was unaffected by the inclusion of the sink terms.

Gasda et al. (2011) and Gasda et al. (2012) include the subgrid convection of CO_2 in a vertical equilibrium formulation (Gasda et al., 2009) using an upscaled representation of the dissolution and convection processes. Like Pruess and Nordbotten (2011), they assume that the convective mixing process begins instantaneously, and that the dissolution rate is linear for all times when gas phase CO_2 is present. Applying this model to some test problems, it was observed that including the enhanced dissolution due to convection could significantly reduce the updip distance travelled by the plume of CO_2, and hence reducing the total time in which the plume is migrating.

Mykkeltvedt and Nordbotten (2012) applied this vertical equilibrium approach to estimate the rate of convective mixing in the Utsira formation at the Sliepner field. This process results in a predicted dissolution rate due to convective mixing of 15 kg m^{-2} y^{-1}, which is comparable to measured estimates. Mykkeltvedt and Nordbotten (2012) note that this relatively high rate of dissolution cannot be explained without including the convective mixing process, suggesting that enhanced dissolution due to convective mixing can be important even during the injection process.

An example of the long-term effect of spatial grid size on the CO_2 dissolution rate can be seen in Figure 7.1 which compares the dissolved CO_2 mass fraction for both a fine-scale and coarse-scale model at the same time. It is clear that the convective mixing process, which is observed in the fine-scale model is not adequately represented in the coarse-scale results. As previously discussed, this results in a significant underestimate of the total dissolved CO_2 in the coarse model in comparison to the fine-scale model.

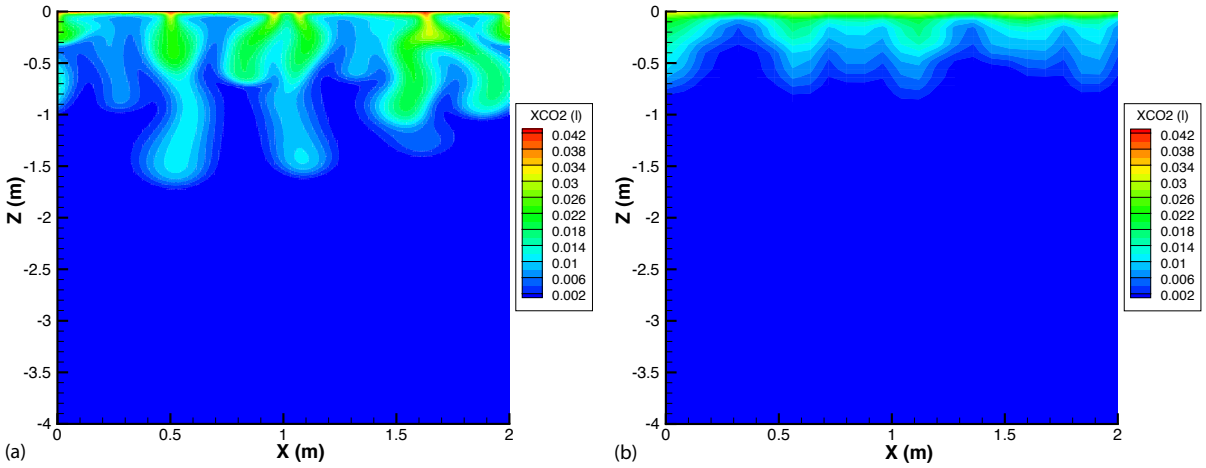

Figure 7.1: Comparison of dissolved CO_2 mass fraction at $t = 5 \times 10^6$ s (approximately 58 days) for (a) fine-scale model with spatial resolution of 0.008 m $\times$ 0.008 m; (b) coarse-scale model with spatial resolution of 0.08 m $\times$ 0.08 m.

In this section, we present a strategy to account for the increased dissolution due to convective mixing in a coarse-scale model through the use of effective reservoir or fluid properties.

7.1 Theory

During the long-term storage of CO_2 in a saline aquifer, the lateral spread of CO_2 beneath a caprock results in a thin region of CO_2-saturated brine lying atop a large body of unsaturated brine, see Figure 2.1. Initially, mass transfer from this saturated brine to the unsaturated brine is purely diffusive. In a fine-scale computational model of this problem, this diffusive transfer is well-resolved, see Figure 7.2(a). In contrast, numerical dispersion due to coarse grid blocks smears this diffusive front, as illustrated in Figure 7.2(b). In particular, the top rows of the fine-scale model accurately capture the saturated CO_2 mass fraction X_0, whereas the top row in the coarse model has an average CO_2 mass fraction that can be significantly smaller than this. As the density difference between brine with and without dissolved CO_2 depends on the CO_2 mass fraction, it is clear that the driving force for density-driven convective mixing is smaller in the coarse model than for the fine-scale model.

The premise of the proposed subgrid correction for convective mixing is that this error is the primary cause of the delayed onset of convection and reduced long-term mass flux observed in coarse-scale models, where the size of the grid blocks are larger than the length scale on which the convective mixing process occurs. To correct this behaviour, an estimate of the error is necessary.

Initially, mass transfer from this saturated brine to the unsaturated brine is purely diffusive, in which case the CO_2 mass fraction $X = C/\rho_b$ in the simplified representation of the problem is

$$X(z,t) = X_0 \operatorname{erfc}\left(\frac{z}{2\sqrt{Dt}}\right), \tag{7.1}$$

where $X_0 = C_0/\rho_b$ is the saturated CO_2 mass fraction and erfc is the complementary error function (Abramowitz and Stegun, 1972). In practice, for numerical simulations of convective mixing, the combination of spatial resolution, diffusivity and onset time of convective mixing results in the argument of the complementary error function in Eq. (7.1) being less than unity.

For small arguments u,

$$\operatorname{erfc}(u) \approx 1 - \frac{2}{\sqrt{\pi}}u + ..., \tag{7.2}$$

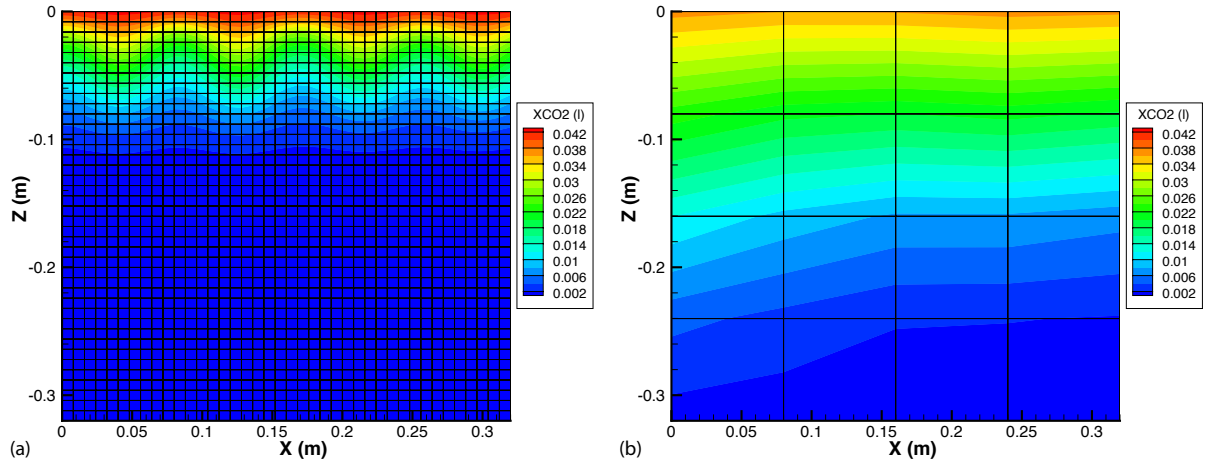

Figure 7.2: Comparison of dissolved CO_2 mass fraction at the onset of convection for (a) fine-scale model with spatial resolution of 0.008 m $\times$ 0.008 m; (b) coarse-scale model with spatial resolution of 0.08 m $\times$ 0.08 m. Note that comparison is at different times due to the delayed onset of convection in the coarse-scale model.

and hence Eq. (7.1) can be well approximated by

$$X(z,t) \approx X_0 \left(1 - \frac{z}{\sqrt{\pi D t}} + ...\right). \tag{7.3}$$

Evaluated at the critical time t_c given by Eq. (4.14) and ignoring any higher order terms, the mass fraction due to diffusion is given by

$$X(z,t_c) = X_0 \left(1 - \frac{kgz\Delta\rho}{\sqrt{c_1\pi}\phi\mu D}\right). \tag{7.4}$$

For small values of CO_2 mass fraction, the difference in the density of the CO_2:brine mixture ρ_m and the original brine ρ_b , $\Delta\rho = \rho_m - \rho_b$, can be well approximated by

$$\Delta\rho \simeq \frac{X\rho_b(\rho_c - \rho_b)}{\rho_c}. \tag{7.5}$$

Substituting Eq. (7.5) into Eq. (7.4) gives

$$X(z,t_c) = X_0\left(1 - \beta X z\right), \tag{7.6}$$

where

$$\beta = \frac{kg}{\sqrt{c_1\pi}D\phi\mu}\frac{\rho_b\Delta\rho}{\rho_c}. \tag{7.7}$$

Rearranging Eq. (7.6) and solving for X, we obtain an estimate of the mass fraction at the onset of convection as a function of vertical distance z

$$X(z) = \frac{X_0}{1 + \beta X_0 z}. \tag{7.8}$$

This result enables the density difference at the onset of convection $\Delta\rho$ to be calculated in an *a priori* fashion using Eq. (7.5), which also enables an estimate of the long-term average mass flux using Eq's. (4.16) and (4.18) for isotropic and anisotropic porous media, respectively, for any vertical spatial resolution Δz.

As $X(z)$ decreases with increasing z, it follows that density difference $\Delta\rho$ will decrease with increasing z. This implies that the long-term average mass flux will also decrease as the spatial resolution is reduced by increasing the computational grid block size (and hence increasing z). Furthermore, compared with the theoretical case ($z \to 0$), the long-term average mass flux for a finite spatial grid ($z > 0$) will be a factor of $X(z)/X_0 = 1/(1 + \beta X_0 z)$ smaller.

Having an estimate for the reduced long-term mass flux due to a finite computational grid enables a grid-dependant correction to be applied. This can be achieved in multiple ways by changing reservoir or fluid properties to balance the predicted decrease in F_m given by Eq's. (4.16) and (4.18) for isotropic and anisotropic porous media, respectively.

In both cases, F_m is estimated to be a factor of $1/(1+\beta X_0 z)$ smaller than the theoretical result. This decrease can be counteracted by increasing one of k or $\Delta\rho$ by an identical amount, or by reducing the viscosity μ by this value. Altering one of these properties has the added benefit of reducing the onset time for convection, see Eq. (4.14), countering the delayed onset observed using coarse-scale grid blocks.

Correcting F_m using this concept also requires the diffusion coefficient D to be scaled in order to keep the mass transfer due to diffusion constant regardless of spatial grid. At the onset of convection ($t = t_c$), the total mass transfer via diffusion is given by (Pruess and Zhang, 2008)

$$m(t_c) = \frac{2\phi^2 \rho_c X_0 D \mu}{\Delta\rho g k} \sqrt{\frac{c_1}{\pi}}. \tag{7.9}$$

Therefore, D should be scaled by a factor of $1 + \beta X_0 z$ in all cases.

7.2 Numerical results

Numerical simulations using TOUGH2 are now presented to demonstrate the proposed correction to the long-term dissolution results. Fluid and reservoir properties used in all simulations are summarised in Table 7.1. The simulation domain used was 2 m in the horizontal direction, and 4 m in the vertical direction. Spatial refinement for the fine-scale (base case) results was 0.008 m in both directions.

Table 7.1: Parameters used in this study.

Pressure, P	11.4 MPa
Temperature, T	59°C
Porosity, ϕ	0.25
Permeability, k	3.95×10^{-12} m^2 (4 d)
Viscosity, μ	0.485×10^{-3} kg m^{-1} s^{-1}
Unsaturated brine density, ρ_0	994.8 kg m^{-3}
Saturated brine density, ρ	1004.7 kg m^{-3}
CO_2 solubility in brine, C_0	44.0 kg m^{-3}
Diffusion coefficient, D	2×10^{-9} m^2 s^{-1}

Figure 7.1 demonstrated that increasing the grid size can significantly reduce the effect of density-driven convective mixing. In that example, the spatial resolution was decreased by an order of magnitude in each direction, so that the computational mesh had grid blocks of 0.08 m in both the vertical and horizontal directions.

Using the theoretical correction presented in the preceding section, grid-corrected parameters can be derived so that the effect of the grid size on dissolution due to convection is reduced. For grid blocks of 0.08 m, the CO_2 mass fraction at the centre of the block (which is where the value is calculated in the TOUGH2 simulator) corresponds to a vertical distance equal to half the grid block

height, i.e., $z = 0.04$ m. The correction factor for this coarse grid can then be calculated using the theoretical model, the calculations of which are summarised in Table 7.2. In this case, the density difference $\Delta\rho$ should be increased by a factor of $X_0/X(z) = 1.8$, which is equivalent to an increase of $\Delta\rho_c = 4.4$ kg m^{-3} at the critical saturation $X(z) = 0.024$, so that the new mixture density is given by $\Delta\rho + \Delta\rho_c$. If the permeability is to be scaled instead, it should be increased by a factor of 1.8. In both instances, the diffusion coefficient should also be scaled by 1.8 to counteract the effect of a coarse grid on the mass transfer due to diffusion at the onset of convection.

Table 7.2: Summary of grid-corrected properties for $\Delta z = 0.08$.

z	0.04 m
β	48.2 m^{-1}
$X(z)$	0.024
$X_0/X(z)$	1.8
$\Delta\rho_c$	4.4 kg/m^3
k	7.11×10^{-12} m^2 (7.2 d)
D	3.6×10^{-9} m^2 s^{-1}

The effect of using grid-corrected properties on a coarse grid is now examined using a computational model with the spatial resolution reduced by an order of magnitude in both directions, so that each grid block is now 0.08 m $\times$ 0.08 m. This corresponds to a reduction in the total number of grid blocks by a factor of 100 for the same computational domain. However, to ensure that the long-term average mass flux can be properly predicted, the total width and height of the coarse-scale model is increased by a factor of 10 in each direction, and only a subsection of the results are shown for illustrative purposes.

Figure 7.3 compares the dissolved mass fraction for the fine-scale 0.008 m $\times$ 0.008 m model, the uncorrected coarse-scale 0.08 m $\times$ 0.08 m model, as well as coarse-scale models with either grid-corrected mixture density or reservoir permeability. As discussed earlier, the use of a coarse grid suppresses the convective mixing process, and the descending plumes of CO_2 that form the convective fingers do not extend as far as for the fine-scale model, which can be observed comparing Figure 7.3(a) and (b). In this case, the coarse-grid blocks are still smaller than the size of the convective fingers, but are not sufficiently refined to properly resolve the convective mixing process.

When the theoretical correction is applied to negate the effect of a coarse grid, larger fingers are observed, as shown in Figure 7.3(c) and (d). In particular, when compared to the uncorrected coarse-scale results in Figure 7.3(b), it is clear that the fingers have reached depths of three to four times that of the uncorrected model, and have grown to a size comparable to that of the fine-scale model, see Figure 7.3(a).

It is interesting to note that the fingers in the corrected coarse-scale models are wider than those of the fine-scale model for both corrections, so that fewer fingers are present in these cases. This is an unavoidable consequence of the larger grid blocks in these models, and occurs due to the lack of grid resolution. In the fine-scale results of Figure 7.3(a), the domain width is split into 250 grid blocks, whereas only 25 grid blocks are present in the same width for the coarse-scale models.

The qualitative comparison between the fine-scale and coarse-scale results (for both uncorrected and grid-corrected cases) can be quantified by examining the mass flux across the top boundary of the model, which are presented in Figure 7.4. The effect of the coarse grid on the rate of dissolution is immediately observed in these results. Convection is observed to occur after approximately 7 days in the fine-scale model, whereas it does not occur in the coarse-scale model until approximately 35 days. Furthermore, over a longer time period, the fine-scale mass flux oscillates about approximately

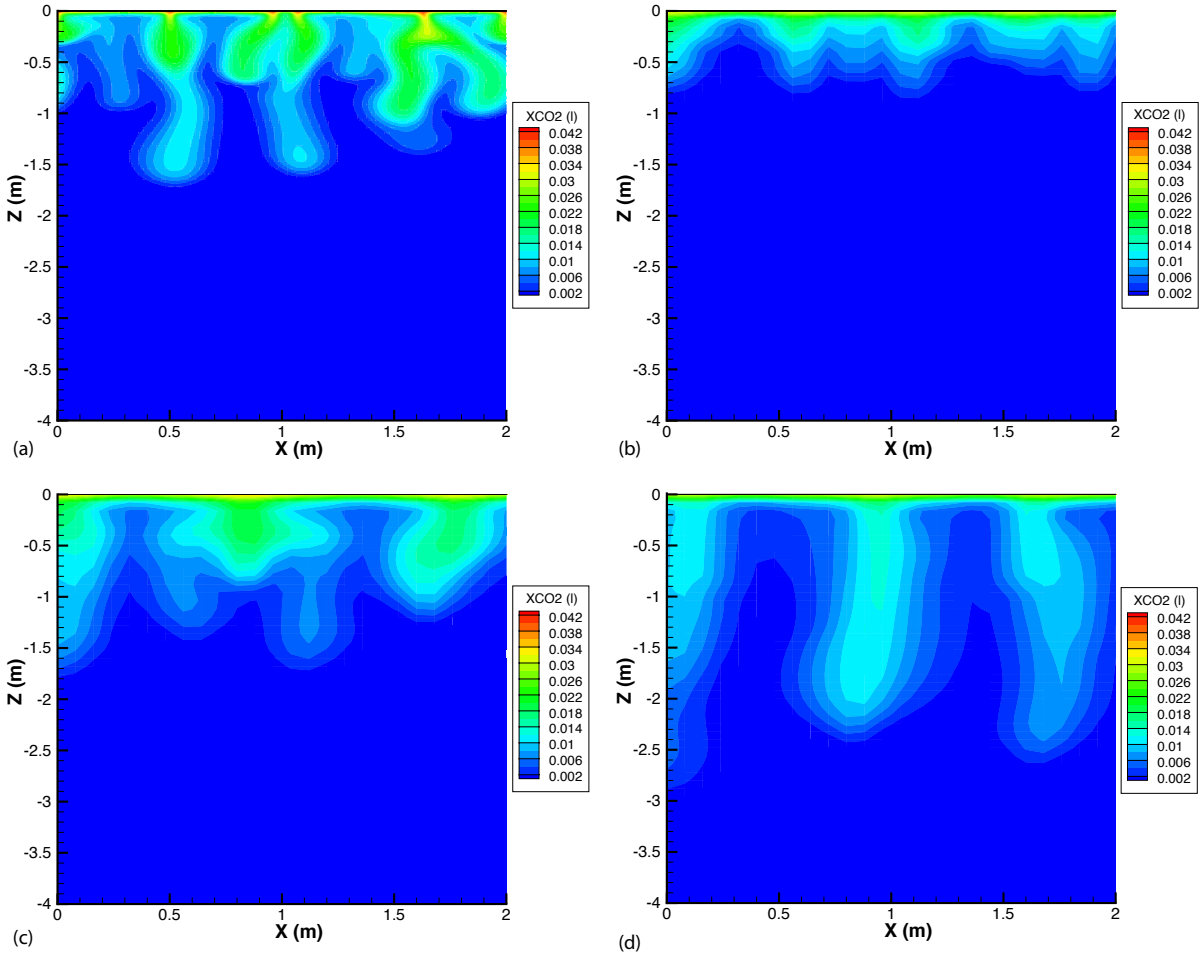

Figure 7.3: Comparison of dissolved CO_2 mass fraction at $t = 5 \times 10^6$ s (approximately 58 days) for (a) fine-scale model with spatial resolution of 0.008 m $\times$ 0.008 m; (b) coarse-scale model with spatial resolution of 0.08 m $\times$ 0.08 m; (c) coarse-scale model with spatial resolution of 0.08 m $\times$ 0.08 m including the mixture density correction; (d) coarse-scale model with spatial resolution of 0.08 m $\times$ 0.08 m including the permeability correction.

5.5×10^{-7} kg m^{-2} s^{-1}, whereas the coarse-scale model levels out quickly at a value of approximately 3.2×10^{-7} kg m^{-2} s^{-1}.

When the grid-dependent density correction is applied, convective mixing in the coarse-scale model now occurs after only 17 days, and the long-term average mass flux is similar to the fine-scale model. If the grid-dependent permeability correction is applied, convection takes place after only approximately 10 days, which is earlier than observed for the mixture density correction. Due to the earlier onset of convection in this case, the long-term average mass flux with the permeability correction is approximately 6.2×10^{-7} kg m^{-2} s^{-1}. This higher value explains the larger fingers observed for this case in Figure 7.3.

It is clear that both strategies for correcting the error in using a coarse-scale grid provide better results than the uncorrected case, suggesting that the theoretical corrections presented in the preceding section can successfully reduce the effects of a coarse-scale grid on predictions of the amount of dissolved CO_2. This can be further examined by comparing the temporal evolution of the total dissolved CO_2, the results of which are presented in Figure 7.5. These results verify that the errors in the total dissolved CO_2 due to the use of a coarse-scale grid can be reduced by using grid-corrected

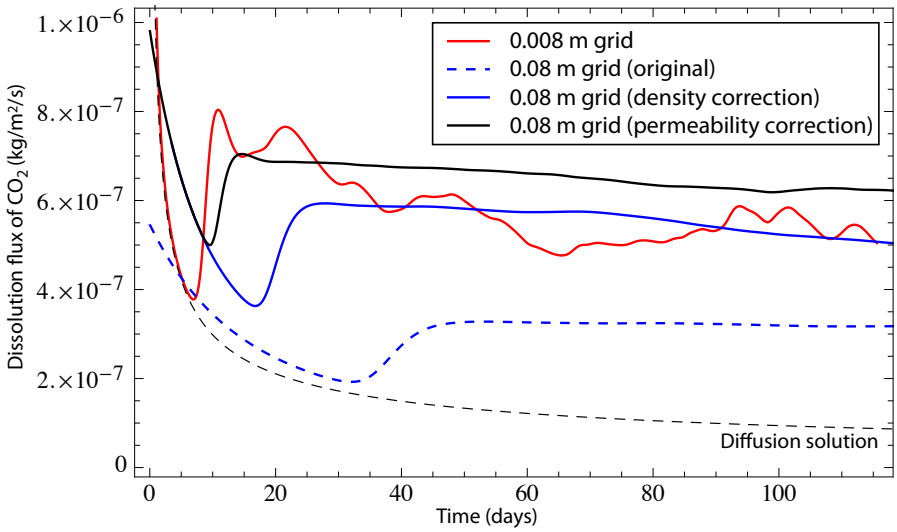

Figure 7.4: Dissolved CO_2 mass flux per unit cross-sectional area. Fine-scale 0.008 m $\times$ 0.008 m grid (solid red line); Coarse-scale 0.08 m $\times$ 0.08 m grid (dashed blue line); Coarse-scale 0.08 m $\times$ 0.08 m grid with grid-dependent density correction (solid blue line); Coarse-scale 0.08 m $\times$ 0.08 m grid with grid-dependent permeability correction (solid black line).

properties.

After 100 days, approximately 5.2 kg m^{-2} of CO_2 has been dissolved for the fine-scale model, compared to only 2.6 kg m^{-2} for the coarse-scale model. This difference is significantly reduced when the density correction is applied to the coarse-scale model, and approximately 4.9 kg m^{-2} of CO_2 has been dissolved, a difference of less than 6%. When using the permeability correction for the coarse model, the total amount of dissolved CO_2 closely follows the fine-scale results up to approximately 50 days, after which they overestimate the amount of dissolved CO_2. After 100 days, 5.6 kg m^{-2} is dissolved using the permeability-corrected coarse model, which corresponds to a difference of 7%.

This example demonstrates that the proposed grid-correction for the long-term mass flux can dramatically reduce the error in the predicted amount of CO_2 that is dissolved in a simulation using grid blocks which would otherwise underestimate the total CO_2 dissolution. However, the coarse grid used is still too refined for a field-scale simulation in practice. We now examine the applicability of the grid-correction scheme for grid blocks that are a factor of 100 times larger in both the vertical and horizontal direction, so that each grid block is 0.8 m $\times$ 0.8 m. Grid blocks of this size could be used in the upper part of a field-scale simulation as part of a local refinement in an area of interest in a irregular computational grid.

Decreasing the spatial resolution by this factor in both directions reduces the number of grid blocks by four orders of magnitude, which leads to a dramatic decrease in computational effort. As before, to properly average the long-term mass flux, the numerical domain is extended in both lateral and vertical dimensions in comparison to the fine-scale case.

Unlike the previous case, grid blocks in this instance are greater than the typical wavelength of the convective fingers, so that convection is now a fully subgrid-scale process. This example will therefore provide a difficult test for the proposed corrections.

Grid-corrected parameters for these coarse grid blocks can be derived using the theoretical model in the preceding section. These are summarised in Table 7.3. In this case, the density difference $\Delta\rho$ should be increased by a factor of $X_0/X(z) = 9.1$, which is equivalent to an increase of 8.8 kg

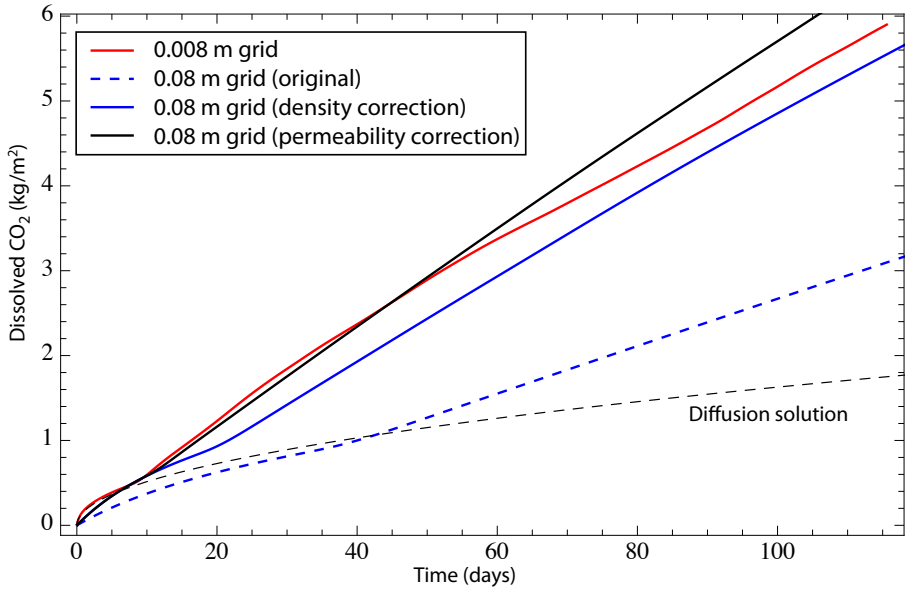

Figure 7.5: Dissolved CO_2 per unit cross-sectional area. Fine-scale 0.008 m $\times$ 0.008 m grid (solid red line); Coarse-scale 0.08 m $\times$ 0.08 m grid (dashed blue line); Coarse-scale 0.08 m $\times$ 0.08 m grid with grid-dependent density correction (solid blue line); Coarse-scale 0.08 m $\times$ 0.08 m grid with grid-dependent permeability correction (solid black line).

m^{-3} at the critical saturation $X(z) = 0.005$. If the permeability is to be scaled instead, it should be increased by a factor of 9.1. In both instances, the diffusion coefficient should also be scaled by 9.1 to counteract the effect of a coarse grid on the mass transfer due to diffusion at the onset of convection.

Table 7.3: Summary of grid-corrected properties for $\Delta z = 0.8$.

z	0.4 m
β	48.2 m^{-1}
$X(z)$	0.005
$X_0/X(z)$	9.1
$\Delta\rho_c$	8.8 kg/m^3
k	3.59×10^{-11} m^2 (36.4 d)
D	18.2×10^{-9} m^2 s^{-1}

Comparisons between the dissolved CO_2 mass fractions for the fine-scale, as well as both uncorrected and corrected coarse-scale models are presented in Figure 7.6 after approximately 100 days. It is immediately obvious that the uncorrected coarse-scale results presented in Figure 7.6(b) does not show indicate any convection at all. In fact, virtually all of the dissolved CO_2 is confined in the top grid block, and only mass transfer by diffusion is observed. This is in stark contrast to the fine-scale results, where significant merging of the convective fingers has occurred, forming large fingers that have descended more than 2 m into the reservoir. The significant suppression of the convective mixing process observed in the coarse-scale model results again highlights how the use of large grid blocks can fail to adequately model the physical processes involved.

Application of the mixture density correction results in large convective fingers on the coarse-scale grid, see Figure 7.6(c). These fingers are longer than those observed in the fine-scale model, but

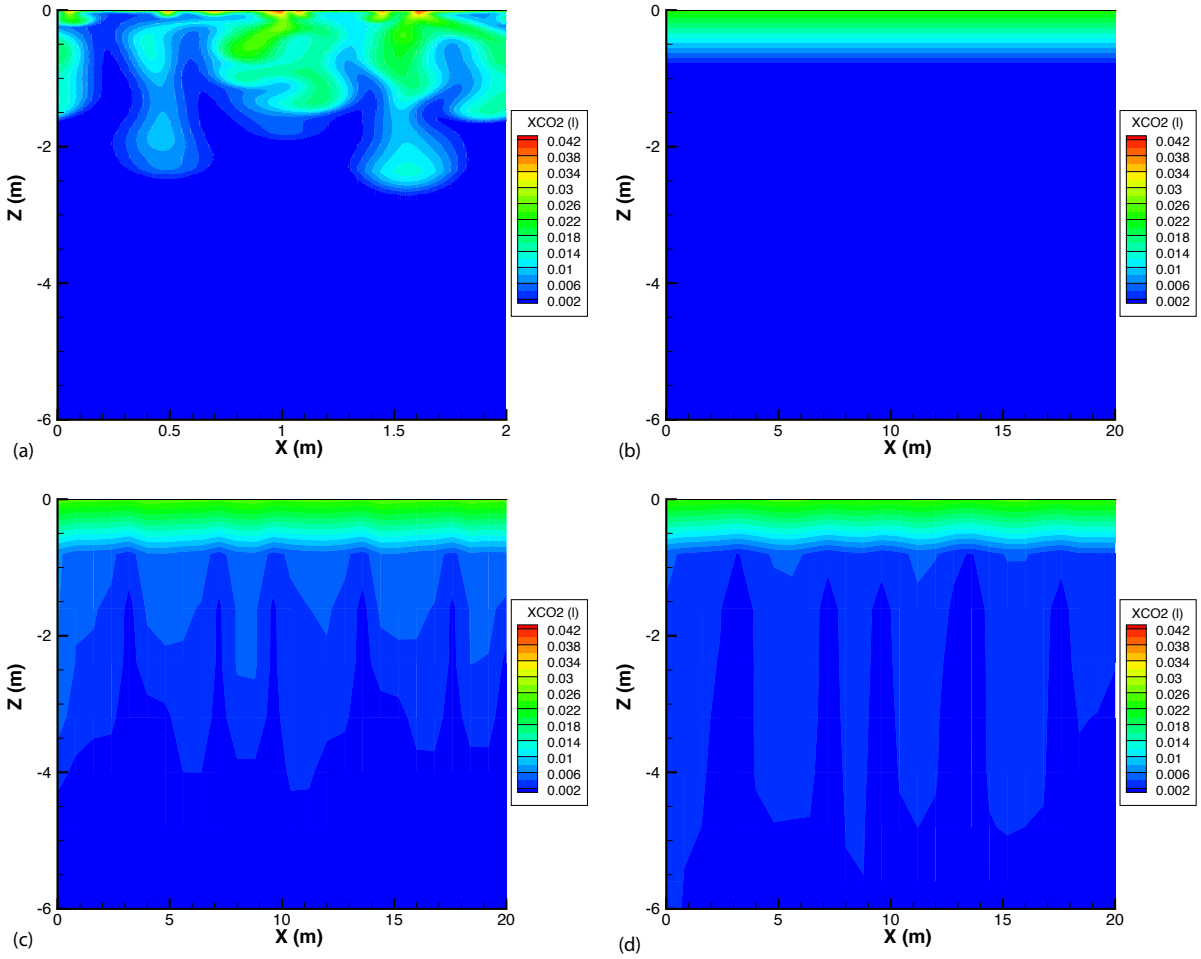

Figure 7.6: Comparison of dissolved CO_2 mass fraction at $t = 8.6 \times 10^6$ s (approximately 100 days) for (a) fine-scale model with spatial resolution of 0.008 m $\times$ 0.008 m; (b) coarse-scale model with spatial resolution of 0.8 m $\times$ 0.8 m; (c) coarse-scale model with spatial resolution of 0.8 m $\times$ 0.8 m including the mixture density correction; (d) coarse-scale model with spatial resolution of 0.8 m $\times$ 0.8 m including the permeability correction. Note the increased horizontal distance for the coarse-scale models compared to the fine-scale model.

have a much lower average dissolved CO_2 mass fraction, suggesting that the amount of dissolved CO_2 is still underestimated in the corrected results. Similar results are observed for the permeability correction, see Figure 7.6(d). In this case, the fingers are larger than the mixture density correction, but the dissolved mass fraction is smaller.

The use of the grid-correction model to improve the coarse-scale results was observed to result in convective mixing where none was observed in the uncorrected coarse-scale model. To assess how well the corrections improve the predictions of the amount of dissolved CO_2, we compare the mass flux for the fine-scale, uncorrected coarse-scale and corrected coarse-scale results, see Figure 7.7. The mass flux for the uncorrected coarse-scale model appears to be almost flat at this scale. This demonstrates that the vertical coarseness of the grid fails to accurately capture even the diffusion process at the top boundary. In comparison to the fine-scale results, the uncorrected coarse-scale results significantly underestimate the mass flux and do not display any convection at all. The uncorrected coarse-scale mass flux is approximately 5×10^{-8} kg m^{-2} s^{-1}, which is approximately one order of magnitude smaller than the long-term average observed for the fine-scale model.

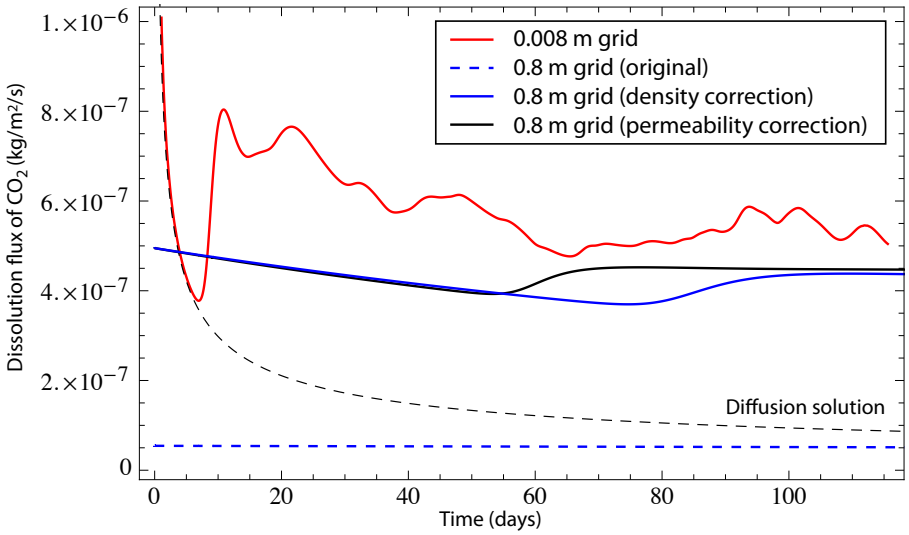

Figure 7.7: Dissolved CO_2 mass flux per unit cross-sectional area. Fine-scale 0.008 m $\times$ 0.008 m grid (solid red line); Coarse-scale 0.8 m $\times$ 0.8 m grid (dashed blue line); Coarse-scale 0.8 m $\times$ 0.8 m grid with grid-dependent density correction (solid blue line); Coarse-scale 0.8 m $\times$ 0.8 m grid with grid-dependent permeability correction (solid black line).

When grid-dependent parameters are used to correct for the spatial coarseness, the initial diffusive mass flux is larger than for the uncorrected model, as expected. Enhanced mass flux due to the onset of convective mixing is observed after approximately 58 days for the permeability correction, and approximately 80 days for the mixture density correction. The long-term mass flux in each of the corrected coarse-scale models is approximately 4.4×10^{-7} kg m^{-2} s^{-1}, which is 20% smaller than the fine-scale model. While not as accurate as for the previous coarse-scale model, these corrected results are a significant improvement on the uncorrected coarse-scale results.

The total dissolved CO_2 for each of these models is compared in Figure 7.8. As expected, the uncorrected coarse-scale model does not adequately predict the amount of dissolved CO_2 at any stage. For example, after 100 days, the fine-scale model predicts that approximately 5.2 kg m^{-2} of CO_2 has dissolved, whereas the uncorrected coarse-scale model predicts that only 0.4 kg m^{-2} is dissolved. This is less than 8% of the fine-scale results, which demonstrates the significant underestimates that can arise using coarse computational grids in this problem.

Both grid-correction schemes considered can be seen to significantly improve the numerical predictions of the total dissolved CO_2 in comparison to the uncorrected coarse-scale model. After 100 days, the coarse-scale model with the mixture density correction predicts that 3.6 kg m^{-2} of the CO_2 has dissolved, while the results with the permeability correction predicts a slightly higher value of 3.8 kg m^{-2} due to the earlier onset time observed for this correction in Figure 7.7. These predictions are at least nine times greater than the uncorrected coarse-scale prediction, and significantly, are only approximately 30% smaller than the fine-scale result, demonstrating that the subgrid corrections proposed in the preceding section can dramatically improve the numerical predictions of the total dissolved CO_2 in coarse-scale models.

An identical scaling can be used for anisotropic homogeneous models to improve the numerical predictions of the total CO_2 dissolution. As the anisotropic homogenous models were observed to be good approximations of the heterogeneous models, it follows that the proposed subgrid corrections can also be applied to upscaled heterogeneous models, at least for the simple heterogeneity considered in this study.

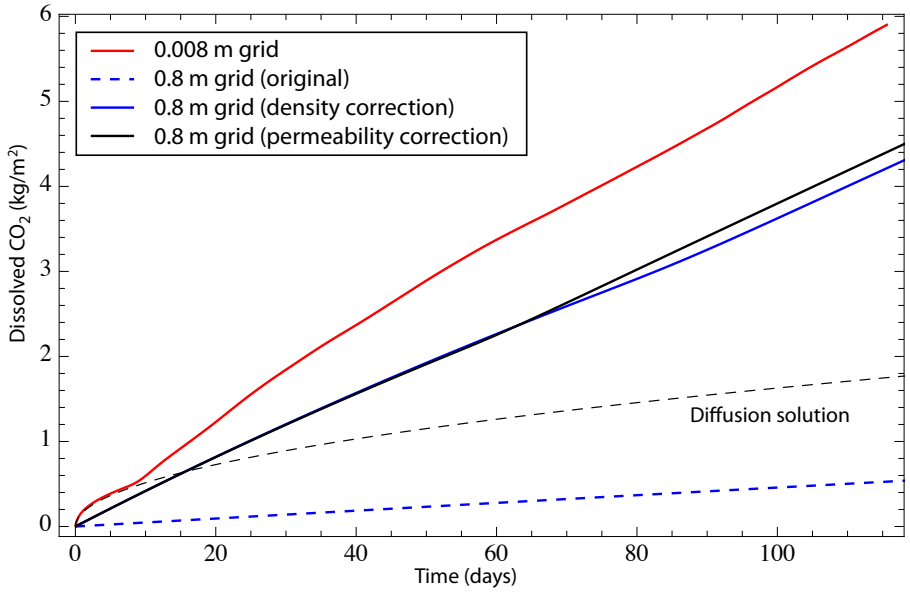

Figure 7.8: Dissolved CO_2 per unit cross-sectional area. Fine-scale 0.008 m $\times$ 0.008 m grid (solid red line); Coarse-scale 0.8 m $\times$ 0.8 m grid (dashed blue line); Coarse-scale 0.8 m $\times$ 0.8 m grid with grid-dependent density correction (solid blue line); Coarse-scale 0.8 m $\times$ 0.8 m grid with grid-dependent permeability correction (solid black line).

The spatial grid correction presented in this section can also be used prior to a simulation to generate a computational mesh that limits the error in the numerical predictions of dissolution due to convective mixing to a given value by estimating the error associated with a particular spatial grid refinement. Previously, a grid sensitivity study would be undertaken to ensure that the mesh was sufficient to adequately capture the dissolution due to convection. This correction can reduce the scope of a sensitivity study by providing an estimate of the error without the need for costly computations. For example, the fine-scale grid used for comparison in this study (0.008 m $\times$ 0.008 m) has an error of less than 5% estimated using Eq. (7.8), which could be deemed sufficient for the problem at hand.

8 Conclusions

Numerical predictions of the amount of dissolved CO_2 during the early stages of a CO_2 storage project, particularly during the injection period where the CO_2 plume grows rapidly, overestimate the actual amount of dissolved CO_2 due to the use of finite-sized grid blocks (Green and Ennis-King, 2012). A simple theoretical scaling based on a geometric argument proposed by Green and Ennis-King (2012) has been used to demonstrate that this discretisation error can be accurately accounted for and effectively removed in numerical simulations.

In the long-term, however, the use of coarse grid blocks in a computational model inhibits the accurate simulation of enhanced dissolution due to density-driven convective mixing, which typically occurs at a spatial length scale that is smaller than the size of the grid blocks necessary in a field-scale simulation due to limits in computational power. In order to improve the long-term numerical predictions of CO_2 dissolution in models that feature large grid blocks, a better understanding of the convective mixing process in heterogeneous reservoirs and the role of geochemical reactions is required.

Using a simple scaling analysis, a theoretical estimate of the average long-term mass flux for convective mixing of CO_2 in an anisotropic saline aquifer was obtained, to complement the available result for isotropic homogeneous reservoirs. The long-term flux for an anisotropic reservoir was shown to scale as $(k_v/k_h)^{1/2}$ times the isotropic estimate, a result that was confirmed using numerical simulations.

A simple heterogeneity model consisting of a random distribution of impermeable horizontal barriers in an otherwise homogeneous porous media was used to demonstrate that an anisotropic model featuring an equivalent effective vertical permeability provided an adequate approximation to the heterogeneous case in terms of the long-term flux, enabling predictions of the long-term dissolution rate in heterogeneous media. The presence of the barriers, however, led to much earlier critical onset times for the heterogenous models than for an equivalent anisotropic homogeneous model.

The coupling of geochemical reactions to the convective flow was also studied. Geochemical effects can increase the dissolution flux by a factor of up to 3, especially when the ion density coupling is included. A geochemical model of the Precipice Sandstone was implemented in TOUGHREACT based on the ANLEC report on the Surat Basin (Haese et al. (2013)). For the Precipice Sandstone, the inclusion of geochemistry increases the dissolution flux due to convection. A means of upscaling these effects was suggested through changes to the fluid density term $\Delta\rho$.

A subgrid-scale scheme for reducing the error in the numerical predictions of long-term CO_2 dissolution due to convective mixing was developed, based on the discretisation error in calculating mass transfer by diffusion and the simple theoretical estimates of long-term mass flux. Several possibilities for implementing the scheme using grid-corrected properties were proposed and assessed using numerical simulations. Comparisons between fine-scale simulations and both corrected and uncorrected coarse-scale simulations demonstrated that by implementing grid-corrected properties, one could significantly reduce the error in the total dissolved CO_2 in a coarse-scale model, even when the size of the grid blocks is increased by two orders of magnitude. For larger grid blocks that may be tens to hundreds of metres in size, such as those that may be used in a field-scale simulation of CO_2 storage in the Precipice Sandstone, the sub-grid correction proposed in this study may not reduce the error in numerical predictions of dissolution to an acceptable amount. In this case, the theoretical estimates and numerical results regarding grid dependence presented may be used to determine the magnitude of the error in numerical predictions when the subgrid scheme is implemented, so that the numerical errors may be reduced within a simulation, while the remaining error is calculated post-simulation. This allows more informed assessment of the numerical predictions to be made.

Most field-scale models of CO_2 storage overestimate dissolution in the short-term, but underestimate

it in the long-term due to the omission of geochemical effects and the coarseness of grids. For storage in the Precipice Sandstone, this leads to an overestimate of the time to dissolved the injected CO_2. This implies that numerical predictions of the amount of CO_2 still in a mobile state is also overestimated. As a result, any simulation predictions regarding possible leakage into the overlying formations should be considered as possible worst-case scenarios.

The results obtained in this project can be implemented in commercial simulation software to improve the modelling of the short-term and long-term behaviour of injected carbon dioxide. Better models (with upscaling of the effects of convection and geochemistry) will reduce the project risk by improving estimates of CO_2 dissolution and long-term storage security.

References

Abramowitz, M., Stegun, I.A., 1972. Handbook of mathematical functions. Dover, New York.

Aggelopoulos, C.A., Tsakiroglou, C.D., 2012. Effects of micro-heterogeneity and hydrodynamic dispersion on the dissolution rate of carbon dioxide in water-saturated porous media. Int. J. Greenh. Gas Con. 10, 341–350.

Andres, J.T.H., Cardoso, S.S.S., 2011. Onset of convection in a porous medium in the presence of chemical reaction. Physical Review E 83, 046312.

Bachu, S., Gunther, W.D., Perkins, E.H., 1994. Aquifer disposal of CO_2: hydrodynamic and mineral trapping. Energy Conserv. Mgmt. 35, 269–279.

Backhaus, S., Turitsyn, K., Ecke, R., 2011. Convective instability and mass transport of diffusion layers in a Hele-Shaw geometry. Physical Review Letters 106, 104501.

Bear, J., 1972. Dynamics of fluids in porous media. Dover Publications, New York.

Begg, S.H., King, P.R., 1985. Modelling the effects of shales on reservoir performance: calculation of effective vertical permeability, in: SPE Reservoir Simulation Symposium, Dallas, Texas, U.S.A., February 10–13. SPE 13529.

Chen, C., Zhang, D., 2010. Pore-scale simulation of density-driven convection in fractured porous media during geological CO_2 sequestration. Water Resour. Res. 46, W11527.

Cheng, P., Besehorn, M., Firoozabadi, A., 2012. Effect of permeability anisotropy on buoyancy-driven flow for CO_2 sequestration in saline aquifers. Water Resour. Res. 48, W09539.

Cinar, Y., Riaz, A., Tchelepi, H., 2007. Experimental study of CO_2 injection into saline formations. SPE J. 14, 588–594.

Dentz, M., Tartakovsky, D.M., 2009. Abrupt-interface solution for carbon dioxide injection into porous media. Transp. Porous Med. 79, 15–27.

Duoxing, Y., Rongshu, e., Deliang, Z., 2011. Numerical simulation of convective stability of the short-term storage of CO_2 in saline aquifers. Int. J. Greenh. Gas Con. 5, 986–994.

Elenius, M.T., 2011. Convective mixing in geological carbon storage. Ph.D. thesis. University of Bergen.

Elenius, M.T., Gasda, S.E., 2012. Impact of tight horizontal layers on dissolution trapping in geological carbon storage, in: XIX International Conference on Water Resources, CMWR 2012, June 17-22.

Elenius, M.T., Johannsen, K., 2012. On the time scales of nonlinear instability in miscible displacement porous media flow. Comp. Geosci. 16, 901–911.

Ennis-King, J., Gibson-Poole, C.M., Lang, S.C., Paterson, L., 2003. Long-term numerical simulation of geological storage of CO_2 in the Petrel Sub-basin, North West Australia, in: Gale, J., Kaya, Y. (Eds.), Addendum to Proceedings of the Sixth International Conference on Greenhouse Gas Control Technologies, October 1-4, Kyoto, Japan, Elsevier Science Ltd.. pp. 11–16.

Ennis-King, J., Paterson, L., 2002. Engineering aspects of geological sequestration of carbon dioxide. SPE Paper 77809 Presented at the 2002 SPE Asia Pacific Oil and Gas Conference and Exhibition, Melbourne, Australia, 8-10 October.

Ennis-King, J.P., Paterson, L., 2003. Role of convective mixing in the long-term storage of carbon dioxide in deep saline formations, in: SPE Annual Technical Conference and Exhibition, 5-8 October, Denver, Colorado, USA. SPE 84344.

Ennis-King, J.P., Paterson, L., 2005. Role of convective mixing in the long-term storage of carbon dioxide in deep saline formations. SPE J. , 349–356.

Ennis-King, J.P., Paterson, L., 2007. Coupling of geochemical reactions and convective mixing in the long-term geological storage of carbon dioxide. Int. J. Greenh. Gas Con. 1, 86–93.

Ennis-King, J.P., Preston, I., Paterson, L., 2005. Onset of convection in anisotropic porous media subject to a rapid change in boundary conditions. Phys. Fluids 17, 084107.

Farajzadeh, R., Ranganathan, P., Zitha, P.L.J., Bruining, J., 2011. The effect of heterogeneity on the character of density-driven natural convection of CO_2 overlying a brine layer. Advances in Water Resources 34, 327–339.

Farajzadeh, R., Salimi, H., Zitha, P.L.J., Bruining, H., 2007. Numerical simulation of density-driven natural convection in porous media with application for CO_2 injection projects. Int. J. Heat Mass Tran. 50, 5054–5064.

Farajzadeh, R., Zitha, P.L.J., Bruining, H., 2009. Enhanced mass transfer of CO_2 into water: Experiment and modelling, in: SPE EUROPEC/EAGE Annual Conference and Exhibition, Amsterdam, The Netherlands, 8-11 June.

Gasda, S.E., Nordbotten, J.M., Celia, M.A., 2009. Vertical equilibrium with sub-scale analytical methods for geological CO_2 sequestration. Comp. Geosci. 13, 435–450.

Gasda, S.E., Nordbotten, J.M., Celia, M.A., 2011. Vertically averaged approaches for CO_2 migration with solubility trapping. Water Resour. Res. 47, W05528.

Gasda, S.E., Nordbotten, J.M., Celia, M.A., 2012. Application of simplified models to CO_2 migration and immobilization in large-scale geological systems. Int. J. Greenh. Gas Con. 9, 72–84.

Ghesmat, K., Hassanzadeh, H., Abedi, J., 2011a. The effect of anisotropic dispersion on the convective mixing in long-term CO_2 storage in saline aquifers. AIChE Journal 57, 561–570.

Ghesmat, K., Hassanzadeh, H., Abedi, J., 2011b. The impact of geochemistry on convective mixing in a gravitationally unstable diffusive boundary layer in porous media: CO_2 storage in saline aquifers. J. Fluid Mech. 673, 480–512.

Green, C.P., Ennis-King, J.P., 2010a. Effect of vertical heterogeneity on long-term migration of CO_2 in saline formations. Transp. Porous Med. 82, 31–47.

Green, C.P., Ennis-King, J.P., 2010b. Vertical permeability distribution of reservoirs with impermeable barriers. Transp. Porous Med 83, 525–539.

Green, C.P., Ennis-King, J.P., 2012. Spatial grid correction for short-term numerical simulation results of carbon dioxide dissolution in saline aquifers. Comp. Geosci. 16, 1153–1161.

Green, C.P., Ennis-King, J.P., 2013. Residual trapping beneath impermeable barriers during buoyant migration of CO_2. Transp. Porous Med 98, 505–524.

Haese, R.R., Horner, K., Kirste, D., Tenthorey, E., Grigorescu, M., 2013. Regional stress and predicted hydrogeochemical impact of CO_2 storage in the Surat Basin - Interim report. Technical Report. ANLEC R & D. ANLEC Ref 3-1110-0088.

Hassanzadeh, H., Pooladi-Darvish, M., Keith, D.W., 2005. Modelling of convective mixing in CO_2 storage. J. Can. Petrol Technol. 44, 43–51.

Hassanzadeh, H., Pooladi-Darvish, M., Keith, D.W., 2006. Stability of a fluid in a horizontal saturated porous layer: effect of non-linear concentration profile, initial, and boundary conditions. Transp. Porous Med. 65, 193–211.

Hassanzadeh, H., Pooladi-Darvish, M., Keith, D.W., 2007. Scaling behavior of convective mixing, with application to geological storage of CO_2. AIChE Journal 53, 1121–1131.

Hassanzadeh, H., Pooladi-Darvish, M., Keith, D.W., 2009. The effect of natural flow of aquifers and associated dispersion on the onset of buoyancy-driven convection in a saturated porous medium. AIChE Journal 55, 475–485.

Hesse, M.A., Riaz, A., Tchelepi, H.A., 2006. Resolving density fingering during CO_2 sequestration: a challenge for reservoir, in: Proceedings, CO2SC Symposium, March 20-22, Berkeley, California, U.S.A., pp. 1–4.

Hesse, M.A., Woods, A.W., 2010. Buoyant dispersal of CO_2 during geological storage. Geophys. Res. Lett. 37, L01403.

Hidalgo, J.J., Carrera, J., 2009. Effect of dispersion on the onset of convection during CO_2 sequestration. J. Fluid Mech. 640, 441–452.

Hodgkinson, J., Grigorescu, M., 2012. Background research for selection of potential geostorage targets—case studies from the Surat Basin, Queensland. Australian Journal of Earth Sciences , 1–19.

Hong, J.S., Kim, M.C., 2008. Effect of anisotropy of porous media on the onset of buoyancy-driven convection. Transp. Porous Med. 72, 241–253.

Jahangiri, H.R., Zhang, D., 2011. Effect of spatial heterogeneity on plume distribution and dilution during CO_2 sequestration. Int. J. Greenh. Gas Con. 5, 281–293.

Javaheri, M., Abedi, J., Hassanzadeh, H., 2010. Linear stability analysis of double-diffusive convection in porous media, with application to geological storage of CO_2. Transp. Porous Med. 84, 441–456.

Javeheri, M., Abedi, J., Hassanzadeh, H., 2009. Onset of convection in CO_2 sequestration in deep inclined saline aquifers. J. Can. Petrol. Technol. 48, 22–27.

Kihm, J.H., Kim, J.M., Wang, S., Xu, T., 2012. Hydrogeochemical numerical simulation of impacts of mineralogical compositions and convective fluid flow on trapping mechanisms and efficiency of carbon dioxide injected into deep saline sandstone aquifers. Journal of Geophysical Research 117, B06204.

Kneafsey, T.J., Pruess, K., 2010. Laboratory flow experiments for visualizing carbon dioxide-induced, density-driven brine convection. Transp. Porous Med. 82, 123–139.

Lindeberg, E., Bergmo, P.E.S., 2003. The long-term fate of CO_2 injected into an aquifer. Greenhouse Gas Control Technologies 1, 489–494.

Lindeberg, E., Wessel-Berg, D., 1997. Vertical convection in an aquifer column under a gas cap of CO_2. Energy Convers. Manag. 38, S229–S234.

Lindeberg, E., Wessel-Berg, D., 2011. Upscaling studies of diffusion induced convection in homogeneous and heterogeneous aquifers. Energy Proc. 4, 3927–3934.

Lu, C., Lichtner, P., 2007. High resolution numerical investigation on the effect of convective instability on long term CO_2 storage in saline aquifers. J. Phys. Conference Series 78, 1742–6596.

MacMinn, C.W., Neufeld, J.A., Hesse, M.A., Huppert, H.E., 2012. Spreading and convective dissolution of carbon dioxide in vertically confined, horizontal aquifers. Water Resour. Res. 48, W11516.

Macminn, C.W., Szulczewski, M.L., Juanes, R., 2011. CO_2 migration in saline aquifers. Part 2. Capillary and solubility trapping. J. Fluid Mech. 688, 321–351.

van der Meer, L.G.H., 1992. Investigations regarding the storage of carbon dioxide in aquifers in the Netherlands. Energy Conserv. Mgmt. 33, 611–618.

Moghaddam, R.N., Rostami, B., Pourafshary, P., Fallahzadeh, Y., 2012. Quantification of density-driven natural convection for dissolution mechanism in CO_2 sequestration. Transp. Porous Med. 92, 439–456.

Mykkeltvedt, T.S., Nordbotten, J.M., 2012. Estimating effective rates of convective mixing from commercial-scale injection. Environ. Earth Sci. 67, 527–535.

Neufeld, J.A., Hesse, M.A., Riaz, A., Hallworth, M.A., Tchelepi, H.A., Huppert, H.E., 2010. Convective dissolution of carbon dioxide in saline aquifers. Geophys. Res. Lett. 37, L22404.

Nield, D.A., Kuznetsov, A.V., 2007. The effects of combined horizontal and vertical heterogeneity and anisotropy on the onset of convection in a porous medium. Int. J. Thermal Sci. 46, 1211–1218.

Nield, D.A., Simmons, C.T., 2007. A discussion on the effect of heterogeneity on the onset of convection in a porous medium. Transp. Porous Med. 68, 413–421.

Nordbotten, J.M., Celia, M.A., 2006. Similarity solutions for fluid injection into confined aquifers. J. Fluid Mech. 561, 307–327.

Nordbotten, J.M., Celia, M.A., Bachu, S., 2005. Injection and storage of CO_2 in deep saline aquifers: analytical solution for CO_2 plume evolution during injection. Transp. Porous Med. 58, 339–360.

Pau, G.S.H., Bell, J.B., Pruess, K., Almgren, A.S., Lijewski, M.J., Zhang, K., 2010. High-resolution simulation and characterization of density-driven flow in CO_2 storage in saline aquifers. Adv. Water Resour. 33, 443–455.

Prasad, A., Simmons, C., 2003. Unstable density-driven flow in heterogeneous porous media: A stochastic study of the Elder[1967b] "short heater" problem. Water Resour. Res. 39, 1007.

Pruess, K., Nordbotten, J.M., 2011. Numerical simulation studies of the long-term evolution of a CO_2 plume in a saline aquifer with a sloping caprock. Transp. Porous Med. 90, 135–151.

Pruess, K., Nordbotten, J.M., Zhang, K., 2009. Numerical simulation studies of the long-term evolution of a CO_2 plume under a sloping caprock, in: Proceedings, TOUGH Symposium 2009, pp. 1–7.

Pruess, K., Oldenburg, C., Moridis, G., 1999. TOUGH2 user's guide, version 2.0. Technical Report LBNL-43134. Lawrence Berkeley National Laboratory.

Pruess, K., Zhang, K., 2008. Numerical Modeling Studies of The Dissolution-Diffusion-Convection Process During CO_2 Storage in Saline Aquifers. Technical Report. Lawrence Berkeley National Laboratory.

Ranganathan, P., Farajzadeh, R., Bruining, H., Zitha, P.L.J., 2012. Numerical simulation of natural convection in heterogeneous porous media for CO_2 geological storage. Transp. Porous Med. 95, 25–54.

Rees, D.A.S., Selim, A., Ennis-King, J.P., 2008. The instability of unsteady boundary layers in porous media, in: Vadasz, P. (Ed.), Emerging topics in heat and mass transfer in porous media. Springer, Netherlands. chapter 4.

Riaz, A., Hesse, M., Tchelepi, H.A., Orr, F.M., 2006. Onset of convection in a gravitationally unstable diffusive boundary layer in porous media. J. Fluid Mech. 548, 87–111.

Simmons, C.T., Nield, D.A., Kuznetsov, A.V., 2010. Effect of strong heterogeneity on the onset of convection in a porous medium: Importance of spatial dimensionality and geologic controls. Water Resour. Res. 46, W09539.

Slim, A.C., Ramakrishnan, T.S., 2010. Onset and cessation of time-dependent, dissolution-driven convection in porous media. Phys. Fluids 22, 124103.

Taheri, A., Wessel-Berg, D., Torsaeter, O., Soroush, M., 2012. The effects of anisotropy and heterogeneity on CO_2 dissolution in deep saline aquifers, in: Carbon Management Technology Conference, 7-9 February, Orlando, Florida, U. S. A., pp. 1–10. CMTC 151345.

Weir, G.J., White, S.P., Kissling, W.M., 1996. Reservoir storage and containment of greenhouse gases. Transp. Porous Med. 23, 37–60.

Woods, A.W., Espie, T., 2012. Controls on the dissolution of CO_2 plumes in structural traps in deep saline aquifers. Geophys. Res. Lett. 39, L08401.

Xu, X.F., Chen, S.Y., Zhang, D.X., 2006. Convective stability analysis of the long-term storage of carbon dioxide in deep saline aquifers. Adv. Water Resour. 29, 397–407.

Yang, C.D., Gu, Y.G., 2006. Accelerated mass transfer of CO_2 in reservoir brine due to density-driven natural convection at high pressures and elevated temperatures. Ind. Eng. Chem. Res 45, 2430–2436.

Zhang, W., Li, Y., Omambia, A.N., 2011. Reactive transport modeling of effects of convective mixing on long-term CO_2 geological storage in deep saline formations. Int. J. Greenh. Gas Con. 5, 241–256.

CONTACT US

t 1300 363 400
+61 3 9545 2176
e enquiries@csiro.au
w www.csiro.au

YOUR CSIRO

Australia is founding its future on science and innovation. Its national science agency, CSIRO, is a powerhouse of ideas, technologies and skills for building prosperity, growth, health and sustainability. It serves governments, industries, business and communities across the nation.

FOR FURTHER INFORMATION

CSIRO Earth Science & Resource Engineering
Jonathan Ennis-King
t +61 3 9545 8355
e jonathan.ennis-king@csiro.au
w www.csiro.au/cesre